Universität Zürich[UZH]

Department of Geography

Using tide gauge observations to infer calving activity at a Greenland outlet glacier

ESS 511 Master's Thesis

Author: Antonin Thelonious Salamin, 18-822-114

Supervised by: Prof. Dr. Andreas Vieli, Armin Dachauer, Andrea Kneib-Walter (andrea.walter@geo.uzh.ch)

Faculty representative: Prof. Dr. Andreas Vieli

24.04.2025

University of Zurich[UZH]

Using tide gauge observations to infer calving activity at a Greenland outlet glacier

ESS 511 Master's Thesis

Author
Antonin Salamin
18-822-114

Supervised by
Prof. Dr. Andreas Vieli
Dr. Andrea Kneib-Walter
Armin Dachauer

Faculty representative
Prof. Dr. Andreas Vieli

May 22, 2025
Department of Geography, University of Zurich

Table of content

List of Figures

List of Tables

Abstract

Iceberg calving plays an important role in the accelerating mass loss of ocean-terminating glaciers worldwide. However, the dynamics and underlying processes of calving remain poorly understood, in part because of the limited temporal resolution of satellite imagery, which restricts the ability to observe individual calving events over extended periods. This study analyses a high-frequency (every 4 seconds), two-year-long (July 2022 to July 2024) record from a tide gauge mounted on the fjord shore of a major tidewater glacier in southern Greenland, the Eqalorutsit Kangilliit Sermiat glacier (EKaS). Tide gauges record water level fluctuations, including those from tsunami waves that follow calving, allowing for the indirect detection of calving events.

Using an automated calving wave detection algorithm, a total of 16'224 calving events were extracted over the 2-year record (729 days) and substantial intra-annual variations were found. Lower calving frequencies were observed during periods of dense ice mélange, mostly in winter and spring, and higher frequencies during summer, but also in the second winter of 2024, when strong foehn winds cleared the fjord of ice mélange. The ice mélange appears to dampen wave propagation, and hence the sensitivity of calving event detection. The correspondence with two additional tide gauge sensors deployed during summer 2024 and alternative detection methods, such as terrestrial radar interferometry and seismics, confirms the reliability of tide gauges as a simple method to detect calving event trends for monthly, seasonal, and inter-annual scales and shows the potential of wave height as a simple proxy for calving event size. Overall, our study highlights the potential to monitor and better understand the calving process with inexpensive, autonomous, and long-lasting tide gauges.

Acknowledgments

Firstly, I want to thank my supervisor, Prof. Dr. Andreas Vieli, for the great opportunity; it wouldn't be possible without his trust and support. I also thank my co-supervisors, Dr. Andrea Kneib-Walter and Armin Dachauer, for their valuable input and encouragement. Their availability, constructive feedback, and constant support were a huge help throughout this journey.
Then, I would like to thank Sebastian, Dominik, Ethan, Diego, and the entire Greenfjord team. Being in the field with all of you was a privilege and your shared knowledge, discussions, and field collaboration were very important to my research. I truly appreciated the team spirit we had on the field together.
I would especially like to thank Marie for her daily help and constant support. Whether through encouraging words or simply being there, your presence made the job lighter and more enjoyable. I am truly grateful for your kindness and patience during this process.
A special thanks goes out to my best reviewers, Lorenzo, Marie, and Sebastian, your comments greatly improved my work. This thesis would not be as clear without your help.

1 Introduction

1.1 Motivation and context

Over the past decades, climate change modified the general behaviour and evolution of the Greenland ice sheet (GrIS). Because of it, the GrIS observed a significant mass loss, due to different factors, such as surface melt, changes in ice flow, and long-term instabilities in the mass balance. Studies have been analysing those processes and found that the ice sheet mass balance is increasingly influenced by surface melt processes, particularly during the summer months, combined with seasonal accelerations in ice flux (Joughin et al., 2008; Bartholomaus et al., 2016). All these processes combined with a continuous retreat of glaciers have contributed to ice loss in the GrIS, as shown in figure 1 (King et al., 2018; Mouginot et al., 2019; Otosaka et al., 2023; Shepherd et al., 2020).

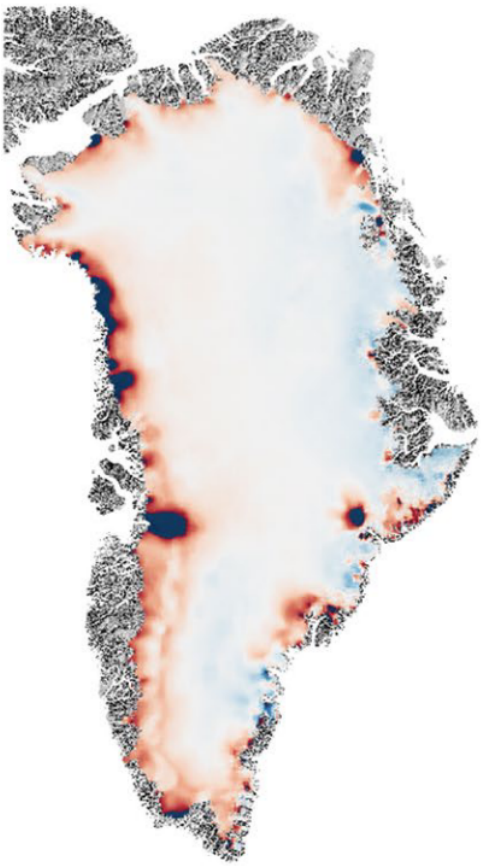

Figure 1: *Greenland Ice Sheet (GrIS) rates of surface elevation change between 2010 and 2021 (Otosaka et al., 2019).*

This loss of ice mass from the GrIS and the acceleration of ice discharge from marine-terminating outlet glaciers contribute significantly to global sea level rise (Enderlin et al., 2014; van den Broeke et al., 2016). The ice sheet contribution is therefore larger than the surface melt alone (Rignot et al., 2011; King et al., 2020). Model projections and field observations suggest that actual changes in ice dynamics will continue to contribute to sea level rise in the future (Morlinghem et al., 2017; IPCC 2019).

The general warming of atmospheric temperatures has increased the sensitivity of GrIS to melting processes (Straneo et al., 2013). This warming, combined with ocean heat fluxes, is accelerating the thinning of the ice cap, and more precisely the periphery of the GrIS (Rignot et al., 2006), which makes the ice sheet retreating (King et al., 2020). Furthermore, raising air temperatures increase meltwater lubrication in the glacier bed, which reduces the resistance to flow (Rignot et al., 2006), disrupting the balance of the glacier.

The fact that tidewater glaciers in Greenland have thinned, retreated, and accelerated in response to environmental change (Enderlin et al., 2014; King et al., 2018) is also related to the geometry and bathymetry of the fjords, with deep fjords hosting steep-based glaciers that demonstrate distinct dynamic responses compared to those terminating in shallow sills (Millan et al., 2018). The variability of glacier responses highlights the importance of local topographic controls in influencing glacier dynamics (Rignot et al., 2006; Catania et al., 2018).

1.2 The process of iceberg calving

Icebergs are produced by a process called calving, which occurs at the front of marine-terminating outlet glaciers. This process occurs primarily due to ice fractures and oceanic melt beneath the glacier's waterline (Minowa et al., 2019). Ice fractures can be triggered by various factors, including stress accumulation within the glacier (Straneo et al., 2013), while oceanic melt is driven by warmer subsurface ocean waters melting the ice from below the water surface (Benn et al., 2017) (see figure 2 for a schematic of the calving process). Furthermore, damaged ice tends to produce smaller and more frequent calving events than large-scale ones (Kneib-Walter et al., 2023). In fjord environments, the stratification of water, often dominated by salinity (Sutherland et al., 2008; Mortensen et al., 2013), plays a crucial role in the thermal dynamics of the fjord water, affecting the rate and nature of calving events. When the sea surface is covered with ice, the temperature tends to be relatively cold. Once the ice melts, by going through a transition phase called ice-mélange, there is a period of warm water lasting about a month. Following this, the temperatures drop again as the icebergs move around, creating a layer of cold freshwater over the saline water, resulting in cold surface water (Mortensen et al., 2013). The interplay between atmospheric temperatures, ocean currents, and tidal patterns further complicates this process, creating a highly dynamic and variable environment in which calving events occur.

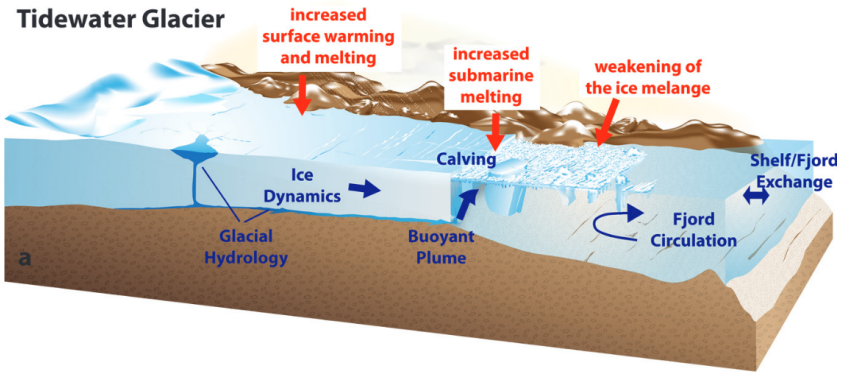

Figure 2: *Schematic of a tidewater glacier (Straneo et al., 2013).*

Understanding calving is essential for several reasons. First, it directly impacts the mass balance of ocean-terminating glaciers and, consequently, global sea levels. As glaciers calve and lose ice mass, they contribute to the rise of sea level (Catania et al., 2020; Kneib-Walter et al., 2021). Secondly, calving can influence the stability and behaviour of glaciers, affecting their flow and potentially leading to more rapid ice loss. The temporal and spatial evolution of the calving front is observed to be controlled by the topography of the bed and fjords and the emergence of subglacial meltwater plumes (Catania et al., 2020). During periods when ice-mélange is present, it has been observed that calving events tend to be less frequent than with free ice, and the glacier front tends to advance (Kneib-Walter et al., 2021). Accurate predictions of calving events are essential for improving glacier models and forecasting future changes in glacier dynamics (Benn et al., 2017) and are important in predicting the long-term impacts of climate change in Arctic regions.

1.3 Theoretical background

While previous studies have provided valuable information on factors that influence calving, several gaps remain in quantifying and modelling calving processes. Until now, most studies on calving have concentrated on monthly to yearly time scales (Bartholomaus et al., 2015; Cassotto et al., 2015; Kneib-Walter et al., 2021), but there is a lack of studies addressing high temporal resolution observations of individual calving events and their variability in space and time (Kneib-Walter et al., 2021).
Current research has identified several environmental forcings that influence calving, including atmospheric temperature, tidal patterns, supraglacial and subglacial hydrology, or submarine melt (Benn et al., 2007; Minowa et al., 2019; Kneib-Walter et al., 2021). However, the complex interactions between these forcing and calving processes remain poorly understood.
The use of indirect methods such as seismic monitoring (Amundson et al., 2012; Bartholomaus et al., 2015; Walter et al., 2020), terrestrial radar interferometry (Walter et al., 2020; Kneib-Walter et al., 2021 and 2023), time-lapse photogrammetry (Jouvet et al., 2017; Minowa et al., 2018), or the analysis of ice mélange (Wehrlé et al., 2023) has provided valuable information but is usually limited in temporal resolution or needs good weather conditions. For example, satellite imageries analyses have a low temporal resolution with a lack of visibility because of the possible presence of clouds. On the contrary, terrestrial radar interferometers (TRI) have a high temporal resolution with detailed volume measurements, but are generally limited to short observation periods, limited during the field campaign (Kneib-Walter et al., 2023). More generally, at the Eqalorutsit Kangilliit Sermiat (EKaS) glacier, South Greenland, several indirect measurement methods have been installed to observe calving (Vieli et al., 2024, Green Fjord, s. d.). More information about the different measurement methods is described in section 1.3.1.
Studies measuring surface water waves produced by calving have highlighted their potential as an indirect method of monitoring calving events (Holland et al., 2016; Lüthi & Vieli, 2016, Minowa et al., 2018). The observation of wave characteristics such as the decay in amplitude over distance, the dependence on the initial height fall of an ice block, and the ice fall behaviour (Heller et al., 2019) can offer some interesting data for inferring the energy and size of calving events (Minowa et al., 2019). However, the effectiveness of methods using wave measurements for detecting small or distant calving events remains uncertain and difficult (Minowa et al., 2019).
Interpreting the wave size time series from the tide gauges might reveal whether in the future, only a temperature and pressure sensor would be needed to determine when it freezes, eliminating the need for image analysis, or if, on the contrary, the temperature and pressure sensor is insufficient. Therefore, this thesis will ultimately contribute towards the development of a methodological approach to continuously monitor calving at high temporal resolution.

1.3.1 Current methods for measuring calving events

To understand and analyse the calving process, many measurement methods can be used. Firstly, modelling can be very interesting, as it allows one to better understand the physical processes and can be expanded to a larger scale, such as the Greenland ice sheet (GrIS). However, high-resolution data for model initialisation and validation are needed, as well as the development of both detailed process models and simple but robust calving laws (Benn et al., 2017).

Other methods include measuring waves transported by the ground, water, or air. Seismic records using seismometers are very accurate in measuring and locating a certain movement of a glacier, or in our case a calving event (Amundson et al., 2012; Bartholomaus et al., 2015; Walter et al., 2020). Submersible and underwater acoustic sensors are another possibility to measure those waves (Deane et al., 2019), as well as infrasounds (Marchetti et al., 2021).
Another possible method is to use terrestrial radar interferometry (TRI) (Kneib-Walter et al., 2021 and 2023), which allows a better understanding of the volume represented by a certain calving event.
In addition, drones, satellites, and time-lapse cameras are interesting to investigate the glacier front using images. Even with a low temporal resolution, such as satellites, this method is useful because no terrain is necessary. On the other hand, drones can provide highly precise images of a glacier as an ortho-image (Jouvet et al., 2017). Lastly, time-lapse imagery can also lead to significant results when synchronised with tide gauge data, for example (Minowa et al., 2018).
Ice-mélange monitoring is another simple method (Amundson et al., 2010). This method looks at the motion of the ice-mélange, its structure, and the size of the icebergs. But wave records produced by calving can also be used to analyse the calving frequency or size distribution, the method chosen in this thesis. The high temporal resolution, the small price of the sensor, the simple installation, and the robustness of the sensor make this method very interesting compared to other methods for long-term analysis. By installing more than one sensor in the fjord near the glacier front, it is possible to compare their detection and extract a lot of valuable information.

1.3.2 Historical knowledge of the EKaS glacier

The Eqalorutsit Kangilliit Sermiat glacier (EKaS), also known as Qajuuttap Sermia in some historical records (Weidick, 2009), was already an object of scientific interest a hundred years ago. Some general descriptions and pictures of the glacier system can be found in the paper of Moltke and Jessen (1896), who documented it during an expedition to the Sermilik Fjord region. Later, Jenkins et al. (1980) emphasised the glacier's hydrological significance, particularly during investigations assessing its potential for hydroelectric power development in the 1970s and 1980s. Then, Weidick et al. (2009) have provided a detailed description of the glacier's fluctuations over the 20$^{\text{th}}$ century (figure 3), explaining that while other glaciers in the same region retreat, the EKaS glacier presented continuous advance from the 1940s until the early 2000s and is considered as the largest expansion of the postglacial time (Weidick, 1995). For the years after, a Nasa simple model computed the evolution of the glacier

Figure 3: *The Eqalorutsit Kangilliit Sermiat (EKaS) glacier in 1942. The glacier front is further back than nowadays (Weidick, 2009).*

front until the year 2024, and the results showed an overall advance until 2024 (Earthdata Search, s. d.). This means that the glacier behaviour did not change after the year 2000, but continued to advance. This interesting behaviour has been linked by Weidick (2009) to local variations in precipitation patterns influenced by the highlands north of Johan Dahl Land. For Millan et al. (2018), this behaviour is an anomaly because other glaciers with a deep fjord such as the EKaS one should be retreating much more.
Since March 2022, a new project has started exploring sociocultural and environmental interactions in South Greenland. It is called the Greenfjord project and is divided into six clusters: atmosphere, ocean, biosphere, cryosphere, human, and land. The cryosphere cluster investigate processes of glacier calving and iceberg export, as well as the resulting hydrodynamics and nutrient fluxes in the fjord (Green Fjord, s. d.). The first trip of the cryosphere cluster occurred in July 2022. From this period, several sensors and instruments (such as time-lapse cameras, weather stations, and a tide gauge) measure the changes that occur on the EKaS glacier and will continue until the end of the Greenfjord project in 2026. This thesis fits directly into this project, since the tide gauge used was installed by Greenfjord in July 2022, during their first field trip.

1.4 Aim of the thesis

This study focusses on the Eqalorutsit Kangilliit Sermiat (EKaS) glacier in southern Greenland, with the aim of improving understanding of calving processes. More precisely, this study investigates the frequency and wave height distribution of calving events over two years of continuous data (from 24$^{\text{th}}$ July 2022 to 22$^{\text{nd}}$ July 2024). The goal when speaking about frequency distribution is to see if temporal patterns on daily, monthly, seasonal, and annual scales emerge and to assess how external forcing factors, such as atmospheric conditions, ocean temperature, precipitation, ice-mélange, tides, and sea ice presence, affect the frequency and the wave heights of calving events. These parameters vary and affect the frequency of calving in different ways, so it is essential to consider them in the analysis.
Sensor data is collected from multiple instruments to help realise this objective. It includes continuous tide gauge measurements, weather station records, and time-lapse camera images. These additional data sets provide complementary information on calving evolution and their relationship to environmental factors. The analyses include statistical and correlation tests between calving activity and external forcing, as well as for frequency and wave height distribution links. This work will also contribute to the methodological development of high-temporal-resolution monitoring systems for glacier calving, based on calving waves measured by tide gauges.

1.4.1 Research questions

This study aims to address three research questions that explore the dynamic behaviour of the Eqalorutsit Kangilliit Sermiat (EKaS) glacier. These questions are as follows.

- How does the frequency and wave height distribution of calving events vary over the 2 years of data?
- On a daily time scale, how variable are the responses of the tide gauges depending on their location?
- How do external factors such as the presence of sea ice (ice mélange), atmospheric conditions, glacier flow variability, and tides influence the frequency and wave height of calving events?
- Methodological question: Is a tide gauge sufficient to monitor calving activity?

Together, these questions will help us to understand the glacier behaviour on a short and long time scale. More precisely, the interactions between calving processes and environmental forcing are analysed to see how they are related.

1.4.2 Hypotheses

To be able to answer the research questions previously exposed, this study is guided by several hypotheses. Regarding the frequency distribution of calving events over long time scale, a distinct seasonal pattern should be visible in the records, with a higher number of events occurring during the warmer months due to a thinner layer of ice present on the fjord sea and warmer temperature.
For the wave height distribution, a higher frequency of small calving events and a comparatively lower occurrence of large-scale events are suggested, due to a highly crevassed glacier (Kneib-Walter et al., 2023).
On a daily time scale, it is expected that the variability in tide gauge signals will be influenced by the local topography, as variations in fjord geometry and bathymetry change the propagation and detectability of calving-induced signals (Vieli et al., 2001; Millan et al., 2018). The precise location of a tide gauge (just behind a boulder, for example) can also change the reception of the signal.
Then, the influence of external forcing factors will be investigated using a number of hypotheses. Wind and ocean temperature are expected to have no direct effect on calving events, as ocean temperature is not changing because of the continuous presence of ice (Mortensen et al., 2013). In contrast, the presence of sea ice, or ice mélange, should attenuate the detection of calving events by damping signals recorded by tide gauges, as it acts as a buffer reducing wave amplitudes. The higher air temperature will also intensify calving activity because of the increase in melt on the glacier.
Lastly, the only use of a tide gauge to monitor calving activity is questioned. The hypothesis suggests that, while a tide gauge could provide valuable long-term records, it would be insufficient for a detailed analysis of individual events.

2 Methodology

2.1 Study area

Eqalorutsit Kangilliit Sermiat (61.33°N, 45.79°W) is a highly crevassed marine-terminated glacier in southern Greenland, north of Qaqortoq. The glacier system covers an area of about 5000 km^2, with 11 % of it forming the ablation area (Weidick 2009). Its front, looking at the fjord from north, is 3.5 km wide, and its height varies between 50 m on the edges and 100 m on the middle part. The glacier rests on bedrock (Millan et al., 2018), composed of granite, biotite, and hornblende-bearing and commonly porphyritic (GEUS Dataverse, s. d.).
The fjord bed is flat, with, 1 km further south of the glacier front, an average depth of approximately 395 m. As no depth sounding can be done at the glacier front, these values have been extrapolated using a boat bathymetry. On the west side of the glacier, a high cliff goes straight down to the flat sea floor, whereas on the east part of the glacier front a small island is present, suggesting a harder bedrock on this side. This island also influences the activity of the calving. Less events occur on the east side of the glacier, while the centre of the glacier front has the most activity recorded. This is mainly due to the variation in speed between the centre and the edges of the glacier, but also to the barrier created by the island in the eastern sector of the glacier.
The glacier's rate of advance evolves and changes according to an almost annual cycle (its live a Nasa Measure Program, s. d.). Its speed varied between 2000 and 3750 m/year over the past 20 years, but in general the glacier front advanced. The reason why it behaves this way is still poorly understood (Millan et al., 2018).

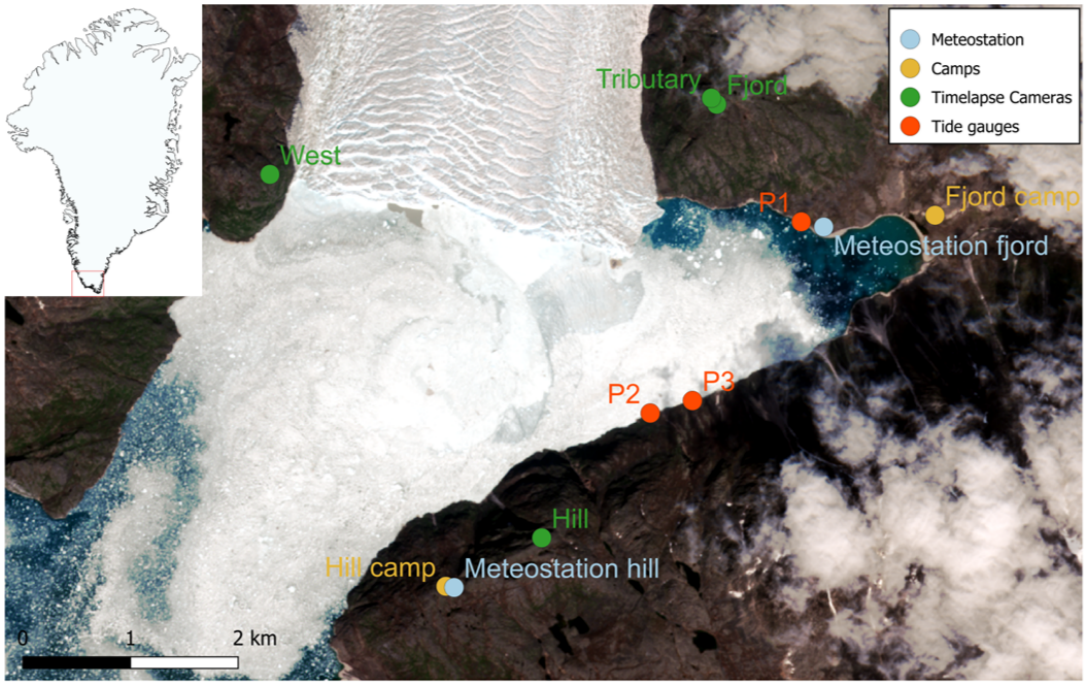

Figure 4: *Field site with all equipment installed and the two base camp location. The equipment is composed of two weather stations (in blue), four time-lapse cameras (in green) and three tide gauges (in red) (MapChart, s. d.).*

2.2 Calving front position evolution

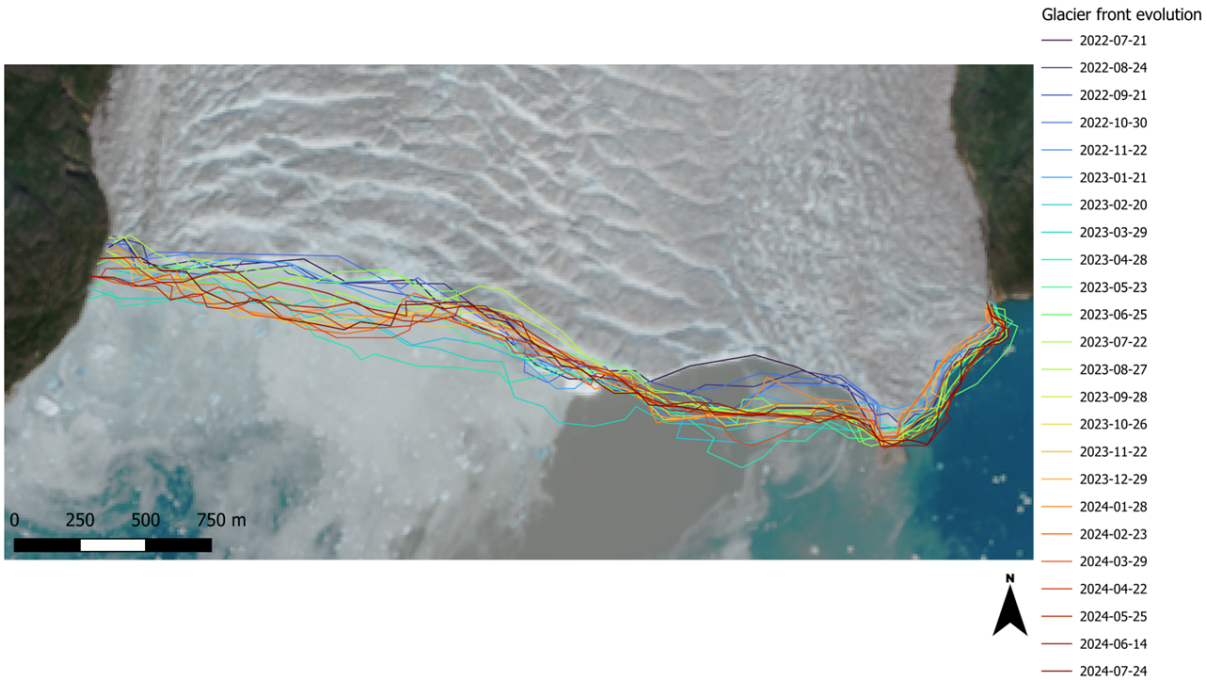

Figure 5: *Monthly evolution of the glacier front position between the 21st of July 2022 and the 24th of July 2024.*

The position of the glacier terminus evolves with calving activity and changes in glacier flow. Interestingly, the glacier front of the EKaS glacier does not retreat as the majority glaciers do in Greenland due to climate change (Catania et al., 2018; Earthdata Search, s. d.), but increased in length between 1953 and 2024 (Weidick, 2009). This behaviour is not visible over the two years of the data set in this thesis, as the time scale is too short.

Figure 5 shows the position of the glacier front each month over the extent of the data set using Sentinel II data (Sentinel Hub, s. d.). This graph was made using QGIS and monthly satellite images to manually draw the front of the glacier. The evolution of the glacier front is as follows: an increase in length during winter (from dark blue to light green) and a retreat during summer (from light green to yellow). Two parts of the glacier front show more changes in the glacier front position, first on the west side of the glacier (left side of the picture) and right on the left from the island (east part of the glacier front). The extreme east part of the glacier front, situated on the right side of the island, has no real changes, except for 25$^{\text{th}}$ June 2023, when the glacier increased slightly more. For the rest of the glacier, on 28$^{\text{th}}$ April 2023 it was the date with the most significant extent in glacier length. It is interesting to note that the greatest extent of the glacier occurred in spring 2023. In contrast, the month with the highest retreat occurred in 21$^{\text{st}}$ July 2022, the first date of the data set. The biggest difference in length between the shortest and the longest month is 431 m and occurred on the west side of the island between the month of July 2022 and the month of April 2023. For comparison, the east part of the island has only a maximum of 183 m difference between the shortest and longest length of the glacier.

The fact that the glacier front remains consistent in length over the two years of data indicates that the distance to tide gauge number 1 (P1) remains constant throughout the

entire dataset. This is a significant advantage as it ensures that the signal intensity is not influenced by variations in distances. Consequently, two signals of the same intensity, one occurring in 2022 and the other in 2024, can be classified as having the same intensity. However, this observation is only valid by ignoring other potential factors that could influence signal intensity. These factors can be the amount of ice mélange present in the fjord, the type of fall, and the initial height fall of an ice block (Heller et al., 2019; Minowa et al., 2019).

2.3 Sensors deployed

Figure 4 shows the location of several instruments and sensors that have been installed around the fjord. Those are time-lapse cameras (green), weather stations (blue), and tide gauges (red). As the project started in July 2022, the instruments and sensors have two years of continuous data, except for the tide gauges P2 and P3, installed in July 2024 for seven days.

2.3.1 Tide gauges

Three tide gauges have been installed around the glacier. The tide gauge, about 30 cm long and 3 cm wide (see figure 7), is placed in a metal tube to protect it from icebergs. Then the metal tube is attached to a boulder on the shore to prevent it from moving, and to get a better record of the waves, as can be seen in figure 6 for P1. A tide gauge measures the water temperature (°C) and the water pressure (dbar). The pressure is directly related to the depth of the water (m), and the tide gauge can convert it into the depth of the water by itself. For an easier understanding, it has been chosen to approximate 1 dbar as 1 m (see Minowa et al. (2018) for more information). Temporal resolution can be modified as needed before installing the sensor.

Figure 6: *Picture of the tide gauge number 1 (P1), placed into a metal tube and screwed to a rock.*

Tide gauge number 1 (P1) was installed in July 2022 during the first field trip of the cryosphere cluster of the Greenfjord project and has a temporal resolution of 4 seconds over 729 days. Some minutes are missing due to the time needed to change the batteries and read out the data from the first year in August 2023. The other two sensors (P2 and P3) were installed during the field trip of July 2024 and have a temporal resolution of 1 second over seven days.
To extract the data from the sensor, the tide gauge is put out of water and the data is downloaded on a computer. The downloaded file with an rsk extension can be read on the programme called Ruskin, and the water temperature, water pressure, and water depth are available.

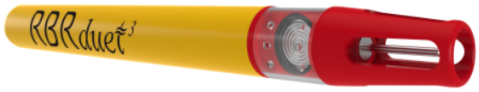

Figure 7: *Picture of the tide gauge sensor (RBR, 2024).*

The side location of the tide gauge P1 is due to the simple access to it. For P2 and P3, the objective was to have the approximative same signal to be able to compare them, and localise a certain calving event. The localisation of individual calving events has not been done because of the time limitation.

2.3.2 Time-lapse cameras

Four time-lapse cameras have been placed around the glacier (see figure 8). Each location was chosen to look at different parts of the glacier, to be able to see different calving events, and to have a better understanding of the calving front, the quantity of ice in the fjord, the plume activity, or the advancing of the glacier itself.
Each time-lapse camera takes an automatic picture every 20 minutes. During the three field trips in July 2022, August 2023 and July 2024, the temporal resolution of the time-lapse camera named "hill" has been increased to 2 minutes and even 1 minute in July 2024.
To extract the data, the routine is to take the SD card and replace it with an empty one, and to make sure that the angle of the camera has not changed during manipulation.
Weather changes (rain, snow, fog), light intensity changes, and dark nights limit the number of pictures that can be used.

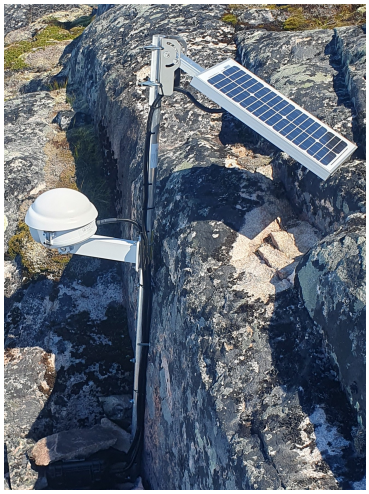

Figure 8: *Picture of the time-lapse camera named hill, near the main camp.*

Figure 9: *Picture of one of the weather stations, near the main camp.*

2.3.3 Weather stations

The two weather stations were installed in July 2022 near the two camps (see figure 9) for easy readability of the data and because the climate is different between the two camps. The "hill camp" has less climatic impact from the glacier, whereas the weather station on the shore has more frequently cold winds. The weather stations measured relative humidity (%), air temperature (°C), solar radiation (W/m^2), and precipitation (mm). In addition to the weather stations installed on the field, the data from the weather station of Narsarsuaq's airport are available (Publikationer Og Rapporter, s. d.). The reason these data were used is that over

30 years of data is in open access and, in particular, wind speed (m/s) and relative humidity (%). Those data are useful to understand whether the warm wind is coming from the glacier, which has a great impact on the quantity of ice present in the fjord.

2.3.4 Other detection methods deployed

Three detection methods are used in this thesis to help understand tide gauge records. Manual observations were made by the Greenfjord team on site, and terrestrial radar interferometry (TRI) and the seismometer were deployed in the hill camp, running continuously.
Manual observations of calving events were made 10 times between 1 and 4 hours continuously, spread over a six-day period from 16th to 21st July 2024. These observations were made from a point of view in front of the glacier using binoculars, to observe calving events. For each observed event, a standardised description was recorded, including an estimated size category, the approximate location along the glacier front (categorised broadly from east to west), and the exact time of the occurrence. Hearing a calving event but not seeing it was not notified as no description of the event could be made. This method provided a great first idea of the size of calving events, which helped to compare certain events with the events recorded by the tide gauge.
The TRI was deployed between 12th and 25th July 2024, and continuously scanned the glacier front from a fixed position. The method is based on radar interferometry, which uses successive radar scans to detect surface displacements and height changes. Operating at high temporal resolution (typically every 1–2 minutes), the TRI captures glacier surface motion and elevation changes in near real time. By differentiating digital elevation models generated from radar returns, it is possible to detect ice loss at the front, identifying calving events with high spatial and temporal precision. This technique allows for the quantification of calving volumes and the analysis of dynamic processes such as crevasse formation, front retreat, and velocity gradients. For more information on how the TRI method works, refer to Kneib-Walter et al. (2023).
Seismic sensors were deployed for a full year to detect calving events based on ground vibrations. For this thesis, two field periods are interesting (28th November to 9th December 2023 and 6th May to 5th June 2024). The instruments were buried in the ground and recorded seismic waves produced by ice detachment and impact. From these data, a range of event parameters can be derived, including the precise time of an event, epicentre coordinates (latitude and longitude), uncertainty of location (dx, dy), duration of the event, and corner frequency (cf). The corner frequency is an interesting parameter, since 1/cf is an approximation of the calving size. The corner frequency is the frequency at which the amplitude of a seismic signal starts to drop, marking the transition between low and high frequencies in the signal spectrum. It is used as an approximation of the size of the calving because larger calving events typically generate lower corner frequencies, reflecting the longer duration and greater energy of the event.

2.4 Data processing

2.4.1 First day of opening of the bay using Satellite images Sentinel II

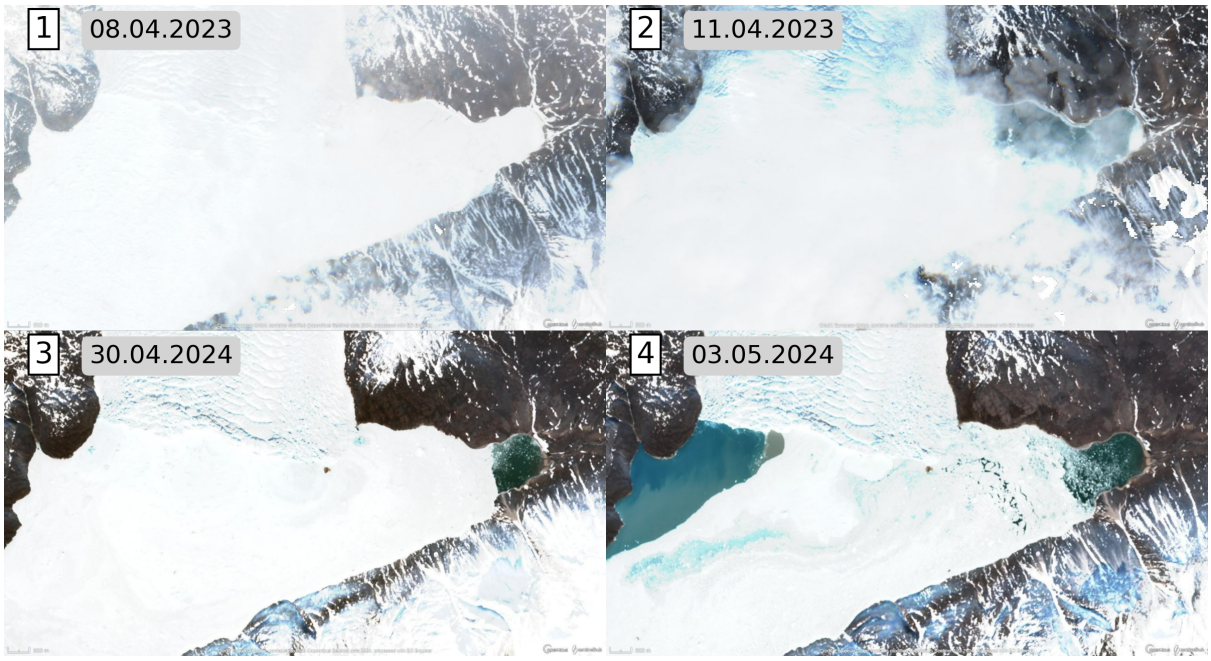

Figure 10: *First opening day of the bay at the location of the pressure sensor 1 (right side of the images). The first year, it occurred between the 8th and 11th of April 2023 (pictures 1 and 2) and for the second year between the 30th of April and the 3rd of May 2024 (pictures 3 and 4) (Sentinel Hub, s. d.).*

To understand the evolution of the frequency of calving events, an important factor is the location of the pressure sensor P1. As it is located in a bay on the east part of the glacier (see figure 4), the quantity of ice mélange present there varies differently compared to the rest of the fjord. The shallower depth of the bay keeps larger icebergs away from it. This creates a barrier that makes the bay have less ice floating there. That is why the bay opened earlier in the year than the rest of the fjord. Figure 10 shows the day of the year when the bay opens for the first time. As we can see in the satellite images, the bay opens while the rest of the fjord is still deeply frozen. Images 1 and 2 show an opening of the bay between the 8$^{\text{th}}$ and the 11$^{\text{th}}$ of April 2023, while images 3 and 4 show an opening between the 30$^{\text{th}}$ of April and the 3$^{\text{rd}}$ of May 2024. The fact that the first day with an open bay is kept in a range of several days is due to a too low temporal resolution of the satellite images of Sentinel II, with a few days within the opening period being too cloudy to be useable.

2.4.2 Data set on the variation in thickness of ice mélange

To perform the analyses, the amount of ice present in the fjord has been a question. Time-lapse cameras have been useful to know the variation of the amount of ice present on the fjord over the two years of data. To keep it simple and easy enough, four categories have been created, with the inspiration of Muckenhuber et al. (2016): "fast ice", "thick ice mélange", "light ice mélange", and "open water". A typical image of each category

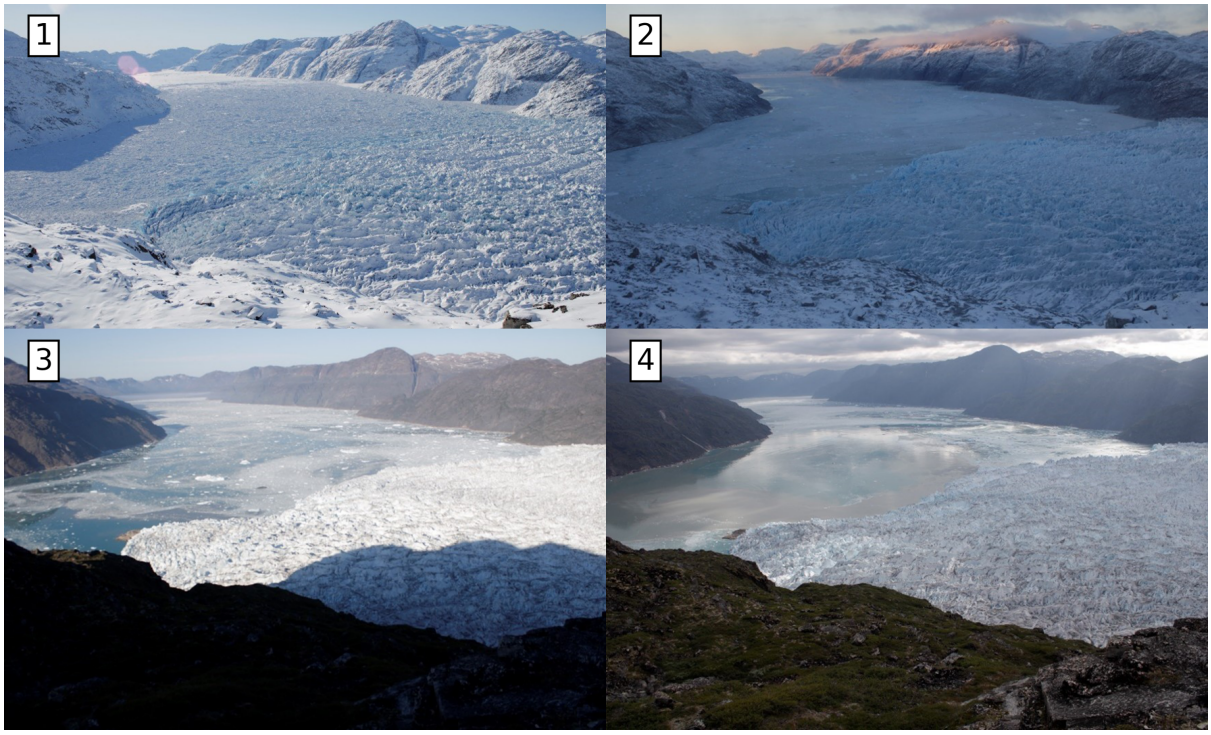

Figure 11: *Typical amount of ice present on the fjord depending on each category. Picture 1 represent "fast ice", picture 2 "thick ice mélange", picture 3 "light ice mélange", and picture 4 "open water".*

is visible in figure 11. To pass from "open water" to "light ice mélange", there should still be some blue patches visible or only a thin layer of ice on the water. The icebergs are still moving freely. Then, to pass into the category "thick ice mélange", the icebergs move slower than with "light ice mélange", and no blue patches are visible on the fjord. If the ice does not move anymore during the day, we pass in the last category, "fast ice". No movement is visible between the shore and the ice mélange.

2.4.3 Data processing parameters

Several steps were necessary to process the tide gauge data and extract a reliable database of calving activity. The analysis focusses on a 7-day reference period (from 15$^{\text{th}}$ July 2024 at 15:30:00 until 21$^{\text{st}}$ July 2024 at 12:00:00), during which the three tide gauges (P1, P2, and P3) were simultaneously recorded. Among these three, only P1 was continuously recorded over a full two-year period and was later used for long-term analysis.
The objective of this processing was to identify and count calving-related peaks in tide gauge records. To do so, a Python script developed by Walter et al. (2020) was used. A high-pass filter of 0.001 Hz was used in the code to first remove the tide influence from the records, so only the calving peaks remain, and the peaks generated by calving activity are still visible. This script can then detect peaks based on two main parameters: a minimum peak height (mph) and a minimum peak distance (mpd) between two consecutive detections.
As a first step, the peaks were manually counted over the 7-day reference period to obtain a preliminary estimate of the number of events. This was done for each tide gauge using

a fixed y-axis scale (-2 to 2 m) to maintain visual consistency. The manually detected number of events was: 85 for P1, 98 for P2, and 110 for P3.
Following this, several combinations of the mph and mpd thresholds (listed in table 5 in the appendix) were tested to reproduce manual counts using the Python script. The best match between manual and automated detection gave 89 events for P1, 96 for P2, and 107 for P3.
To improve the scientific robustness of the mph threshold, manual observations of calving events conducted in the field were used (see section 2.3.4). The events were categorised into six groups: very small, small, medium, large, very large, and huge. Only four of the eleven "very small" events observed in the field matched tide gauge signals, with an average height of 0.0133 m. "Small" events had a better correspondence between manual observations and tide gauge records and an average height of 0.0428 m. For reference, the smallest events detected by manual peak counting had a height of 0.0847 m.
In addition to field observations, TRI (Terrestrial Radar Interferometry) data were also used to cross-check tide gauge records (see section 3.5.1). Among the 31 events detected using TRI, seven events were not detected by the tide gauges. Those seven events were also extremely small (average height: 0.0166 m), in line with the "very small" field category. They were not considered either, as their size is very close to that of the "very small" events in the manual observations.
Based on the comparison with both field and TRI observations, the mph threshold was adjusted to 0.002 m. With this value, the smallest detected peak for each tide gauge during the 7-day period was 0.04 m, consistent with the "small" event category. To maintain a similar relative difference in detection counts between P1, P2, and P3 as in manual counting (difference of 13 between P1 and P2, and a difference of 12 between P2 and P3), mpd thresholds were set as follows: for P1 300 pixels, for P2 600 pixels and for P3 800 pixels. The differences between each tide gauge slightly changed, but stayed in the same range. Ultimately, the thresholds used for each tide gauge record are summarised in the table below (table 1).

Tige gauge	Mph threshold	Mpd thresholds	Nbr of events
P1	0.002	300	140
P2	0.002	600	162
P3	0.002	800	176

Table 1: *Summary of the thresholds used for each tide gauge in the python code. The two thresholds are the minimum peak height (mph) and the minimum time between two detections (mpd).*

Finally, using the selected thresholds (table 1), calving activity was extracted from the entire two-year data set recorded by P1. A high-pass filter of 0.001 Hz was applied again to remove tidal signals. A total of 16'224 events were detected, corresponding to an average of 22.26 events per day for 729 days. Although the amount of ice mélange and iceberg coverage in the fjord varied over time, the same thresholds were applied consistently throughout the 2 years to ensure comparability and avoid introducing seasonally biased thresholds.

2.4.4 Threshold sensitivity

To illustrate the sensitivity of the thresholds used in the python code to extract the calving events, a few results using different thresholds are compared in figure 12. The upper graph shows the daily number of calving events detected by the code with a fixed minimum peak height (mph) and a variable minimum time between two detections (mpd). The blue curve, with an mpd of 300 is the one used for the final code extraction (see table 1). The higher the mpd threshold, the smoother the curve over the entire dataset. The range between the highest and lowest number of calving events detected is highly diminished. Concerning the second graph, the mpd threshold is fixed, while the mph fluctuates. The blue curve is the same as the upper graph for a better comparison of the effect of each threshold modification. In this lower graph, a lower mph threshold shifts the curve upwards and the range between the highest and lowest number of calving events detected increases.

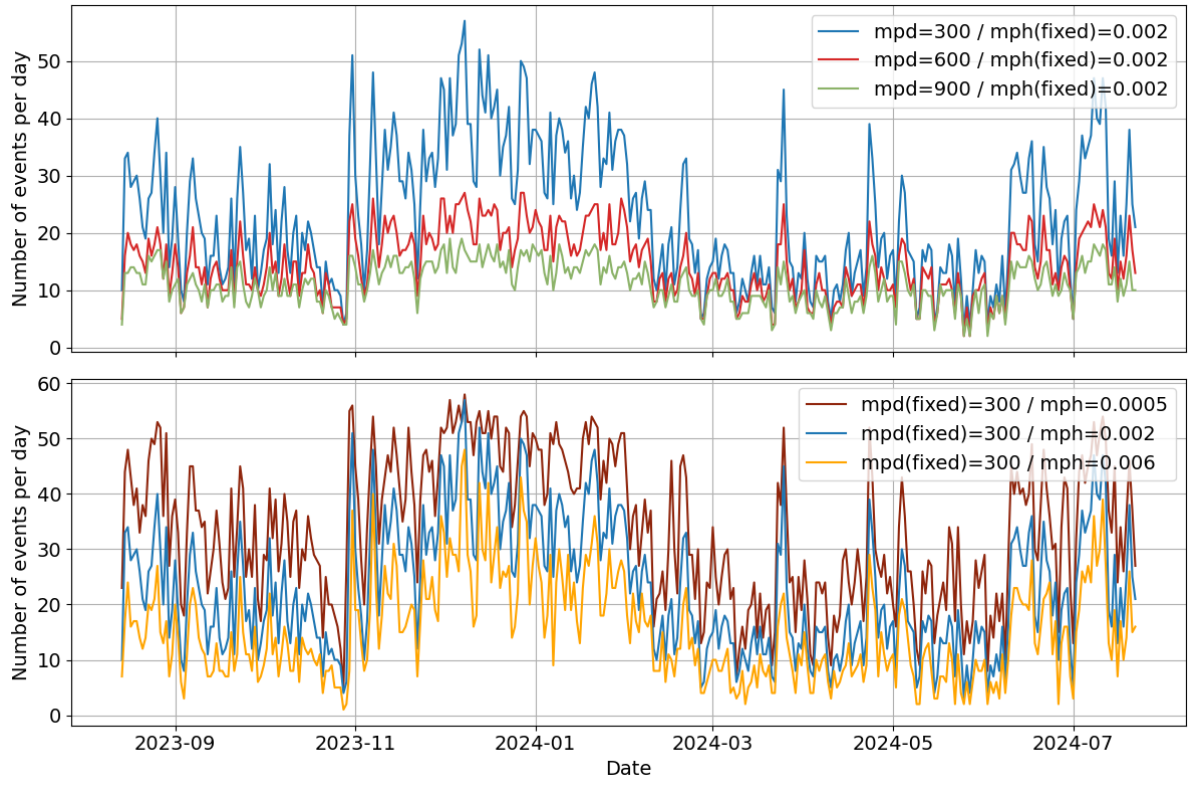

Figure 12: *Sensitivity of the thresholds for conducting the data processing. Visual representation of the two thresholds used in the python code (mpd and mph), with a fixed minimum peak height (mph) in the first graph, and a fixed minimum time between two detections (mpd) in the second graph. The time scale is only a part of the dataset, going from July 2023 to July 2024 for a better visualisation of the curve fluctuations.*

3 Results

This chapter is divided into several sections. The first section outlines the frequency distribution of the calving events, looking at long- and short-time-scale changes. In the second part, the size distribution is presented, also over long and short time scales. In the next part, a comparison between the number of calving events and the wave height evolution is presented. Then, the effects of external forcing factors are described. Ultimately, a comparison between tide gauge data and three other detection methods is evaluated (TRI data, manual observation, and seismic data).

3.1 Calving frequency distribution

3.1.1 Long timescale analysis using the tide gauge P1

The number of calving events detected can vary depending on the season, the month, and the day. This section describes the frequency distribution over those time scales, using data from the tide gauge P1.

3.1.1.1 Seasonal distribution

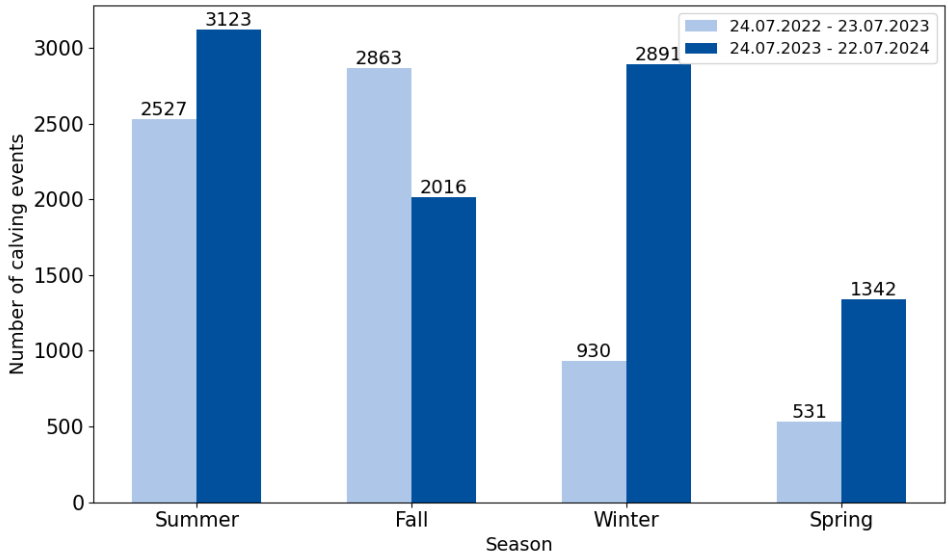

Figure 13: *Number of calving events seasonally distributed separated into two years. Each year starts in July, the 24th July 2022 for the first year (in light blue) and the 24th July 2023 for the second year (in dark blue).*

Concerning the seasonal distribution, some differences are visible within the first (August 2022 to July 2023) and the second year (August 2023 to July 2024), but also between the two years. The first year, visible in light blue in figure 13, has the most events detected during the fall 2022, with 2863 events. In contrast, only 531 calving events occurred in spring 2023. For the second year, visible in dark blue in figure 13, a smaller difference is visible between the biggest season in terms of the number of calving detected and the smallest. 3123 calving events occurred in summer 2024, while only 1342 of them occurred

in spring 2024.
Spring is the season with the lowest number of calving events detected in both years. The season with the closest gap between the two years is summer, with a difference of 596 events. On the opposite, the season with the most differences is winter, with 1961 more events detected during winter 2023-2024 than during winter 2022-2023. Lastly, the only season where the first year has more events detected is fall, with 847 more events detected during fall 2022, mainly due to the month of September (see figure 14).

3.1.1.2 Monthly distribution

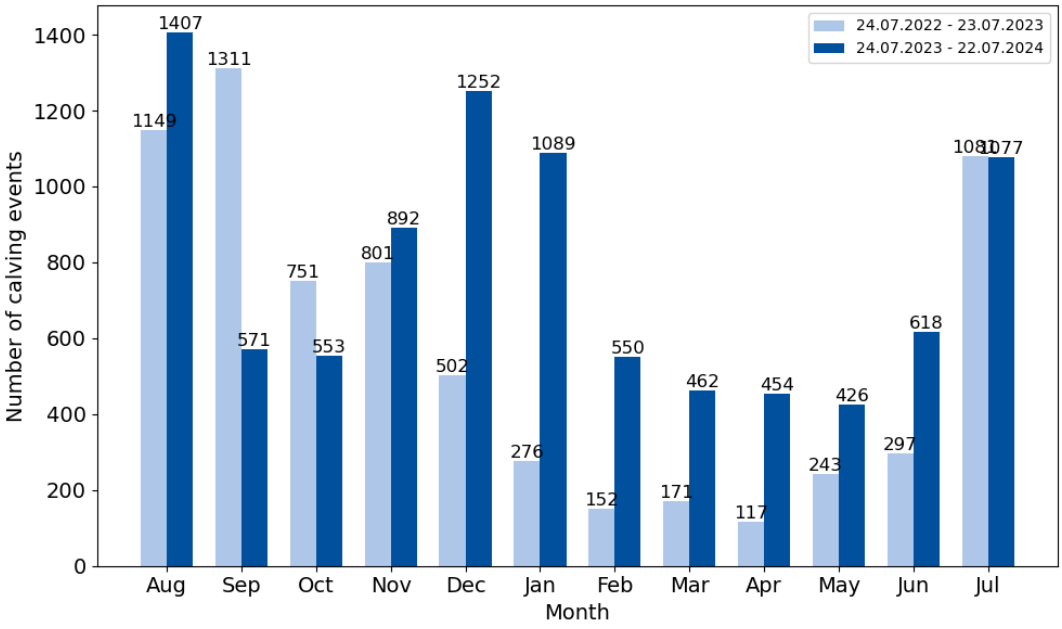

Figure 14: *Number of calving events monthly distributed divided into two years. Each year starts in July, the 24th July 2022 for the first year (in light blue) and the 24th July 2023 for the second year (in dark blue).*

The distribution of calving events over the months changes over the course of a year, but also between the two years of data. During the first year (August 2022 to July 2023) visible in light blue on figure 14, the number of calving events detected changes in each month. July, August, and September have the most events detected, with on average 1'180 events detected during the three summer months. In contrast, February, March, and April have the fewer events detected, with on average 146 events per month.
For the second year (August 2023 to July 2024), the behaviour is slightly different. The three months with the most events detected are August, December, and January. On average, the number of events detected during these months is 1'249. However, the three months with the least detection are March, April, and May. Here, the number of events detected on average for these months is 447, significantly more than for the three months with the lowest occurrence of calving in the 1st year. Interestingly, the evolution of the calving activity between the two years evolves differently. In September, December and January, the differences in terms of number of calving are higher, with a difference of, respectively, 740, 750, and 813 events between the two years of the same months.

3.1.1.3 Daily distribution

An analysis of the number of calving events that occur during the day compared to the night has been carried out to see if any differences are visible in the records. 8'630 events have been detected during the day and 7'593 events during the night. This difference was found to be significant using both the Chi-squared and binomial tests (p-value equal to 0.0 for both tests), suggesting an influence of temperature on calving activity.
In addition to this analysis, the number of calving events detected during early morning (4 a.m. until 12 a.m.) and late afternoon (4 p.m. until 12 p.m.) have been conducted. The number of events that occur during the morning is 4'524, and 4'796 during late afternoon. The differences have also been tested using Chi-squared and binomial tests, and came out significant, even though the p-values are higher (0.0048 and 0.005 respectively), which correlate with the previous suggestion about the temperature influence, as the highest temperature during a day occurs during the afternoon.

3.1.2 Short time scale analysis using the tide gauges P1, P2 and P3

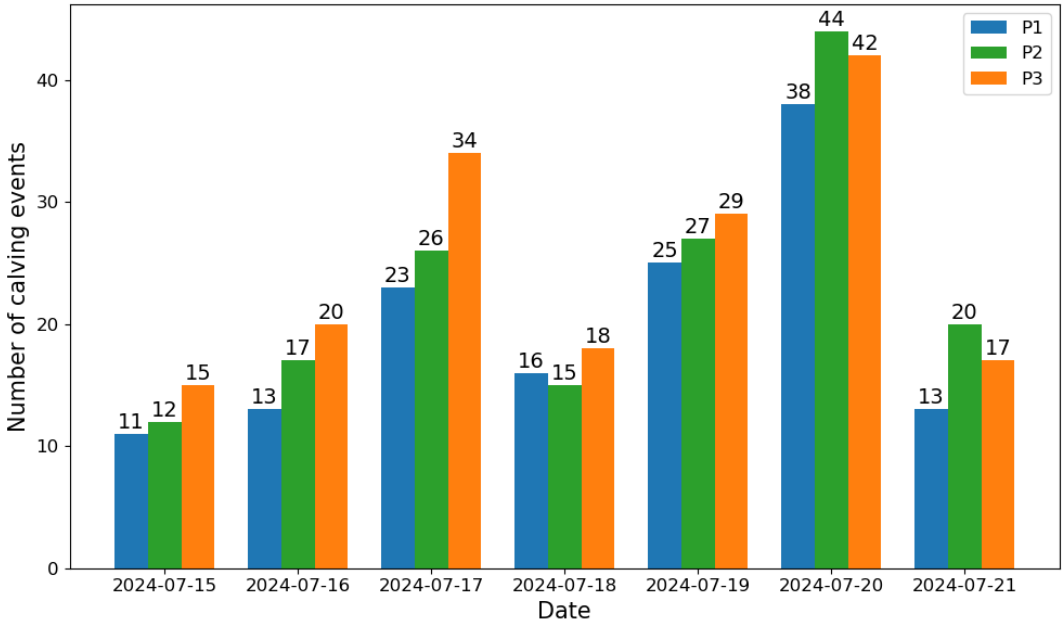

Figure 15: *Daily number of calving events detected by P1 (in blue), P2 (in green) and P3 (in orange) over the 7 days of overlapping data (15.07.2024 - 21.07.2024).*

The number of calving events detected can vary over days, but also between tide gauge sensors. Figure 15 presents the differences between the three tide gauge records, depending on their location. In general, the number of calving events detected by P3 (in orange) is higher than P2 (in green), which itself is higher than P1 (in blue). In addition, P1 always recorded the least number of calving events, except for 18th July, where P2 recorded the least number of events. This trend changes on 20th July 2024 and 21st July 2024, with P2 having the most recorded events.
The biggest gap in terms of the number of events occurred on 17th July 2024, with 11 more events for P3 than for P1. The highest number of calving events detected for each tide gauge occurred on 20th July 2024, with 38, 44, and 42 events detected for P1, P2,

and P3, respectively. This same behaviour highlights a more active day in terms of the number of calving events compared to the rest of the week.

3.2 Wave height distribution

3.2.1 Long time scale analysis using the tide gauge P1

Figure 16 illustrates the wave height distribution and their cumulative wave heights for each month, separated into two graphs, one for each year (the first year on the left and the second year on the right). For this figure, the events detected on 13th July 2023 at 07:21:52 (with a wave height of 2.54 m) have been removed because of an unusual shape in the record (and no calving event is visible at this date on the time-lapse camera). The tide gauge at this time was out of water half of the time when this event occurred, due to the combination of low tide and large waves. The first year (24.07.2022 to 23.07.2023) has a shorter range of wave heights and fewer cumulative wave heights compared to the second year (24.07.2023 to 22.07.2024). In terms of ranges, the wave heights of the first year go from 0.045 to 1.69 m (in November 2022), and its cumulative wave height has a maximum of 175.5 m corresponding to September 2022. The second year has a range of wave heights of 0.039 to 2.12 m (in May 2024), and a maximum cumulative wave height of 280.7 m corresponding to December 2023.

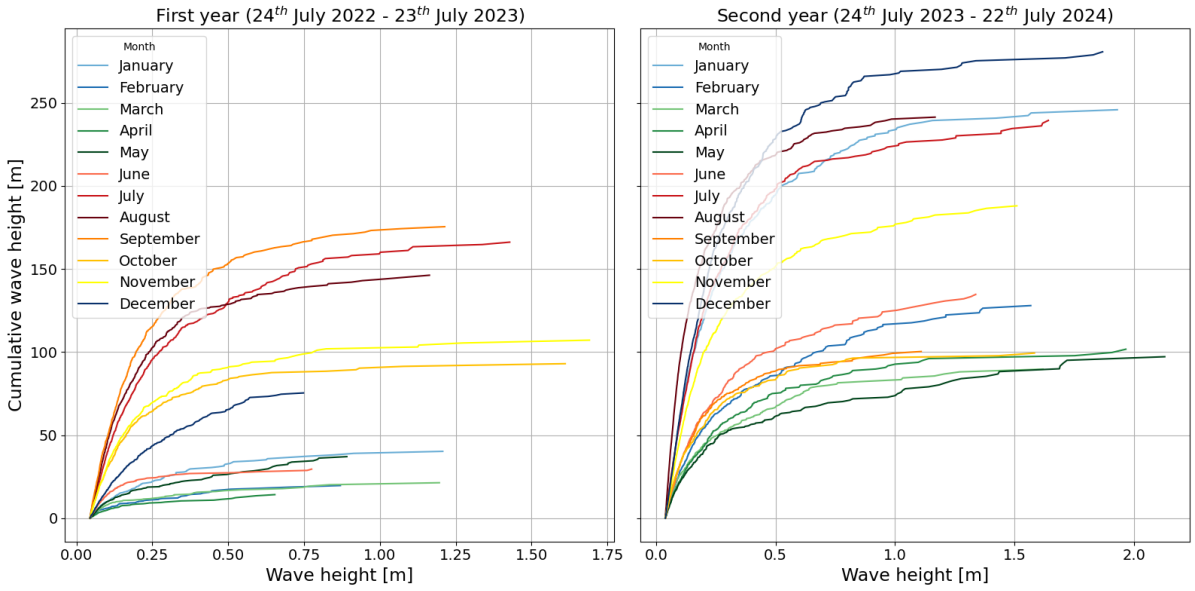

Figure 16: *Cumulative wave height distribution of calving events for each month of the first year on the left (24.07.2022 - 23.07.2023) and second year on the right (24.07.2023 - 22.07.2024).*

The two years have some similarities. March and April had less recorded calving activity, June, July, and August have generally more events cumulatively, and September, October, and November are in between.
In contrast, the first and second years differ in December, January, and February. These three months had a very different wave height maximum (around 0.8 m for the first year

against 1.5 m for the second year), and the cumulative eave height was significantly higher in the second year (around 250 m and only around 50 m for the first year).

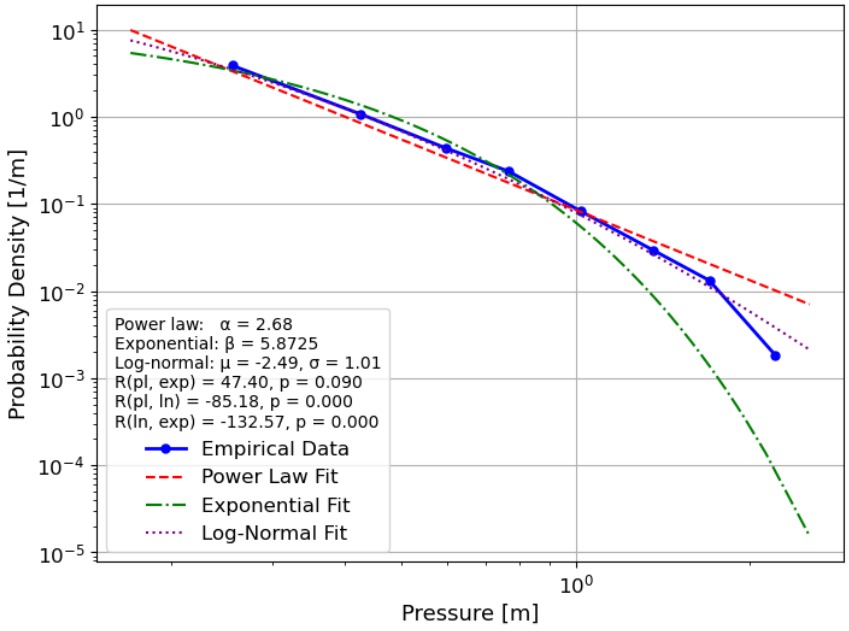

Figure 17: *Probability density function (PDF) method of calving events. The blue curve corresponds to the empirical data, the red curve to a power law fit, the green curve to an exponential fit, and the purple curve to a log-normal fit (Alstott et al., 2014).*

In addition to figure 16, figure 17 illustrates the probability density function (PDF) method of calving events (Alstott et al., 2014). The PDF gives a representation of how the values within a dataset are distributed. It describes the likelihood that data points fall within a specific range for any given interval. Globally, the blue curve shows that much more small events (left side of the graph) are present in the data set, with the y-axis indicating how frequently different wave heights occur in the data set. It is a stationary process that takes all events and sort them by height. To see if the curve behaves as a power law, three curves have been tested: power law, exponential, and log-normal.
Some parameters have to be defined to fully understand this graph. The parameter α is the exponent of the power-law distribution (see equation 1). It determines how steep the tail of the distribution falls off. A lower α (α close to 2) indicates a heavier tail (more extreme values are more probable), while a higher α (α close to 3) means the tail drops more quickly. Concerning the parameter λ, this parameter is the rate for the exponential or truncated power law distributions (see equation 2). β is the exponent in the stretched exponential distribution (see equation 3). It controls how quickly the tail of the distribution decays: when β is equal to 1, it becomes a pure exponential, while β lower than 1 means that the tail is heavier than exponential but lighter than a power law. Lastly, μ is the mean of the logarithm of the values in a log-normal distribution (see equation 4). In the fourth equation, σ is the standard deviation.

$$p(x) \propto x^{-\alpha} \tag{1}$$

$$p(x) \propto x^{-\alpha} e^{-\lambda x} \tag{2}$$

$$p(x) \propto x^{\beta-1} e^{-\left(\frac{x}{\lambda}\right)^{\beta}} \tag{3}$$

$$p(x) = \frac{1}{x\sigma\sqrt{2\pi}} \exp\left(-\frac{(\ln x - \mu)^2}{2\sigma^2}\right) \tag{4}$$

Most importantly, R is the log-likelihood ratio between two fitted candidate distributions. It measures which distribution is a better fit for the data. If R is greater than 0, the first distribution is a better fit, while if R is lower than 0, the second distribution is better. In the algorithm from Altsott et al. (2014), the equation R looks like this:

$$R,\, p = \texttt{fit.distribution\_compare('power\_law', 'exponential')} \tag{5}$$

The statistics show that the power law distribution is not the best fit because a few big events highly influence the best-fit curve. With an α of 2.68, larger calving events are less frequent but still significant, which is consistent with a heavy-tailed distribution. In addition, the p-value of 0.09 is too high to be statistically significant. Considering an exponential fit, with a λ of 2.81 this model underestimates the likelihood of extreme events compared to the power law. Finally, the log-normal distribution is a better model than the power law, because of a negative R (-85), but the exponential model fits better with an R of -132. This tells us that the exponential model is statistically preferred to describe the dataset in this paper, even if the power-law model fits the dataset relatively well. In general, what is interesting in this graph (figure 21) is that this glacier calves significantly more small events than big ones.

3.2.2 Short time scale analysis using the tide gauges P1, P2 and P3

To illustrate the distribution of wave heights depending on the location of a certain tide gauge, figure 18 shows that most calving events are the smallest, visible in the first bin of the graph, under 0.17 m in wave height. In total, 139 events have been detected by P1, with 72.1 % of them being in the first bin. For P2, 161 events have been detected, with 62.7 % of them being in the first bin. For P3, 175 events have been detected, with 62.3 % of them being in the first bin.
The number of events detected by each tide gauge in each category does not vary more than a difference of 11. It also appears that some events from the highest bins were not detected by each tide gauge, which is due to the location and local topography effect. It can happen that the same event is stored in a different bin as the wave can propagate differently. This can explain why tide gauge number 1 has more events in the first bin than in the higher bins.

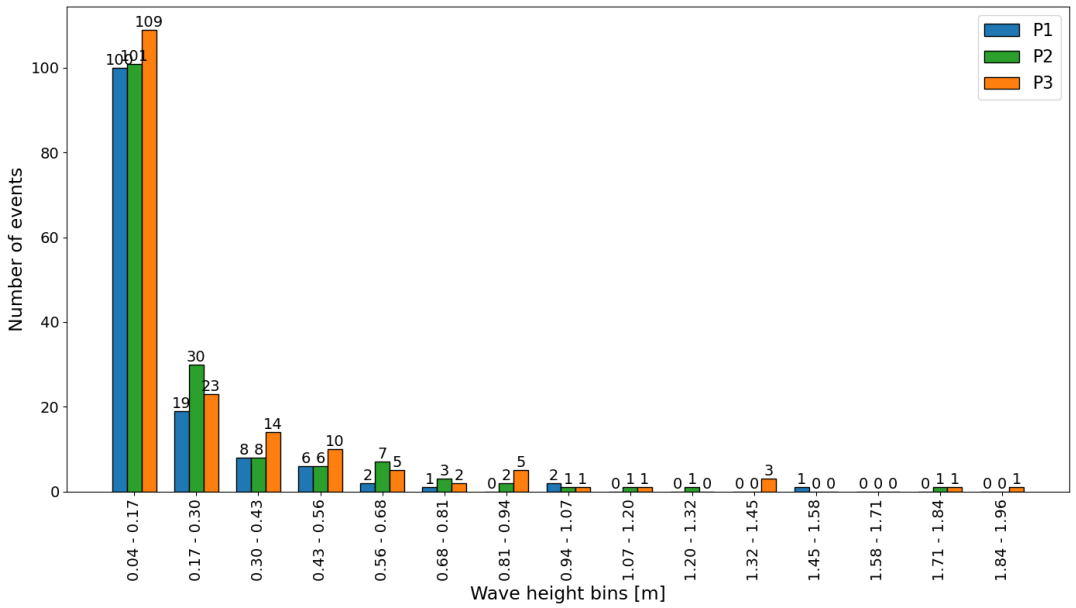

Figure 18: *Wave height distribution of calving events of the three tide gauges in 10 bins for the 7 days of record (15.07.24-21.07.24). P1 is in blue, P2 in green and P3 in orange. The number of calving events recorded in each bin is written on top of each bar.*

3.3 Calving frequency evolution comparison to wave height

This section investigates potential relation between calving frequency and wave height over the two years of data from the tide gauge P1.

3.3.1 Long time scale analysis using the tide gauge P1

Figure 19 illustrates the number of calving events detected daily over the two years of data in blue, and the daily average wave height in red. The number of calving events varies depending on the months and seasons, as described in section 3.1.1. Several periods with distinctly higher numbers of calving events are visible. The first period starts in August 2022 and ends in December 2022 with around 45 detections per day. The second period starts in July 2023 and ends in August 2023 with up to 140 events detected. The third period is between mid-October 2023 and January 2024 with around 40 detections per day, and the last period from June 2024 until the end of the data set (22nd July 2024) with around 35 detections per day. On 8th and 10th August 2023, the exceptionally high number of calving events detected (128, 140) is a period with more waves than usual, which may explain why there is such a difference in the detection compared to the other periods.
In contrast, the daily average wave height evolution does not vary very much over the two years of the data set. It is stable in a range of 0.1 to 0.25 m, with three exceptions: first, on 10th March 2023 the average wave height increased significantly to 0.76 m because only two large events have been recorded (1.19 and 0.32 m), which increase the daily average wave height. Similar peaks in wave heights occur in May 2023 and in May 2024 (both up to 0.4 m). However, in general, there seems to be no clear relationship between the average daily wave height and the number of calving events (see figure 20).

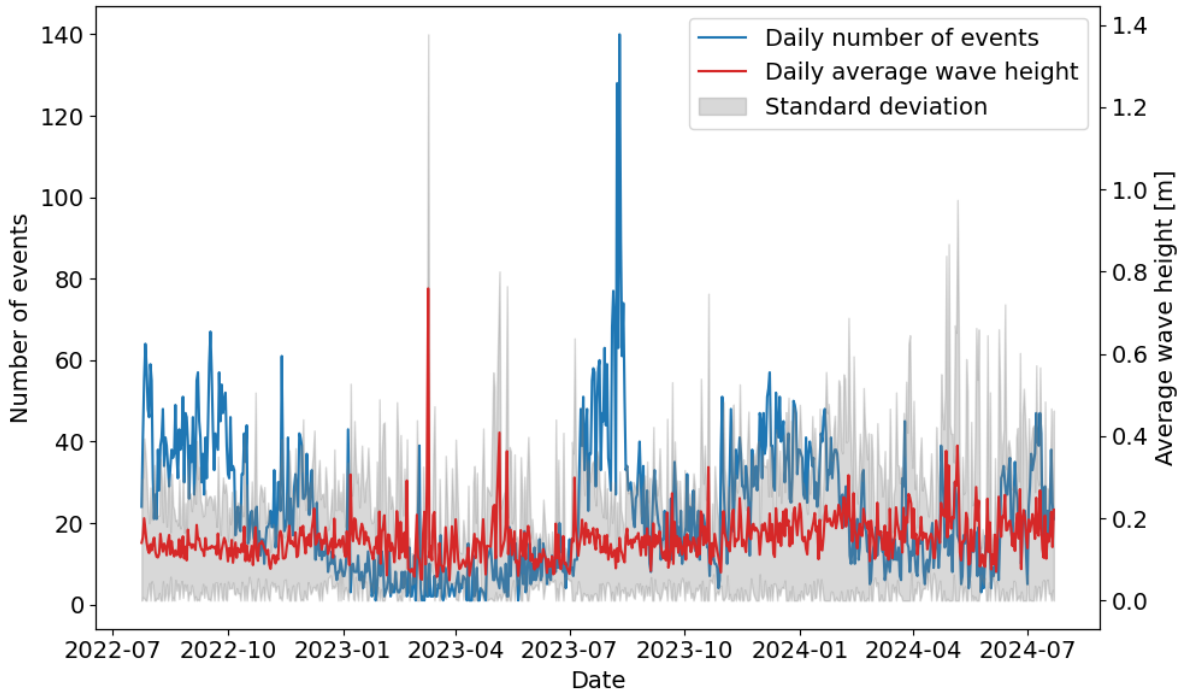

Figure 19: *Daily average number of calving events detected in blue and daily average wave height in red over the two years of data. The uncertainty of the average wave height is in grey.*

3.3.1.1 Monthly comparison between wave height and frequency

The link between wave height and the number of events can highlight the dynamics of each season. Figure 20 shows the number of calving events that occurred in each month compared to the average median wave height of these events. The two study years (08.2022 - 07.2023 and 08.2023 - 07.2024) are coloured green and blue, respectively.
Looking at the variation in the number of calving events, three main groups can be identified. Each group consists of the same months for the two periods. The first group, composed of February, March, April, May, and June, visible as two blue circles, has the lowest number of detected calving events. The second group is coloured yellow and is composed of October and November. The last group in red is composed of July and August, with the exception of July 2024 that behaves like the yellow months. The four months of January, July, September, and December have a very different behaviour between the two years, which is why there are not categorised in any group (grey). July 2023 is still categorised in the red group because of the similarities with its next month, August 2023 and are both summer months.
Concerning the wave height of the events, there is an overall trend to have a higher wave signal in the second year than in the first one. Except for September and August, all months show an increase in the median wave height for the second year. Removing this effect from consideration to see more clearly, two clusters can be categorised. Those clusters are not directly visible in figure 20, but the goal here is to illustrate a tendency. The first group, with the smallest median on average, is composed of March, May, and October (both years). The second, with a higher median, is composed of July, November, and December (both years). As an exception, February, April, and June (both years) appear to have a small median wave height during the first period and a higher one

during the second period. Meanwhile, August has a lower median wave height in the second year, and September does not reveal any changes. The September dynamic can be explained because of a longer or shorter summer period depending on the year, which is why the number of calving events detected vary a lot.

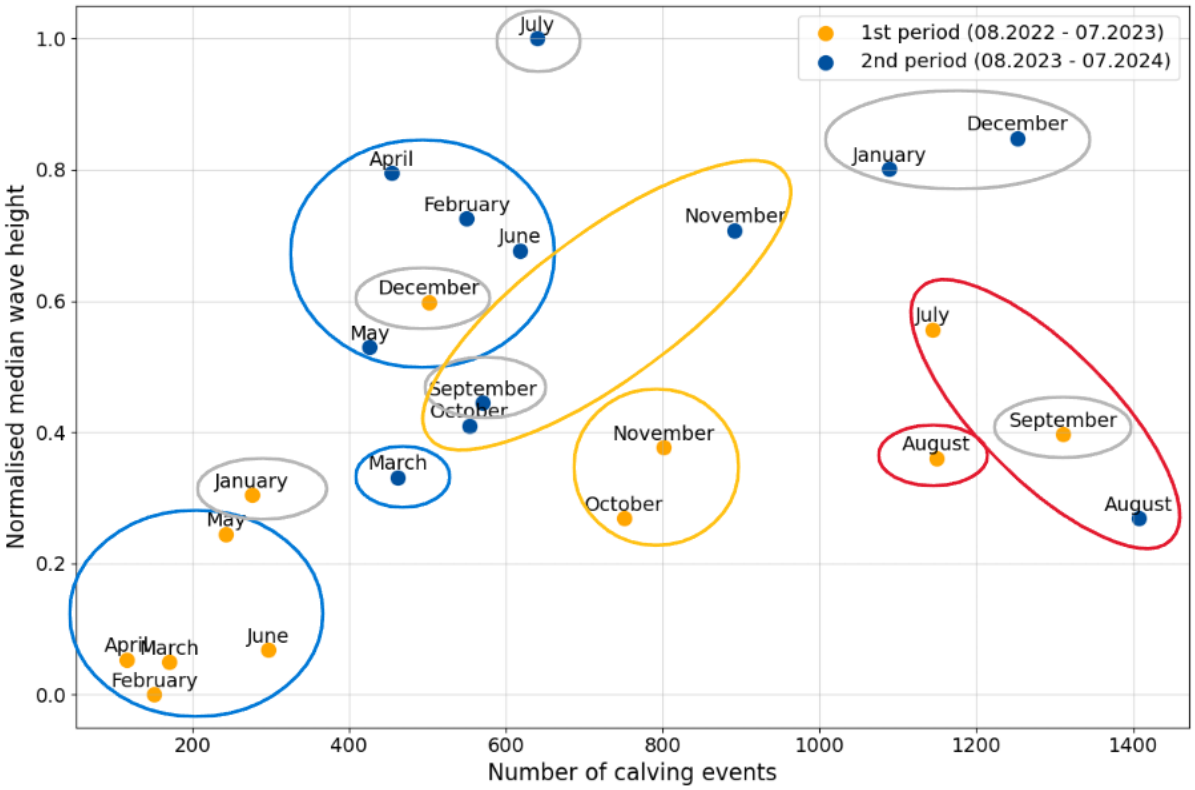

Figure 20: *Monthly variability in number of calving events on the x-axis compared to the monthly median wave height of those calving events on the y-axis. The first year is visible in orange and the second one in blue (08.2022 - 07.2023 and 08.2023 - 07.2024). The blue, yellow and red circles categorises the number of calving events depending on the months. The grey circles highlight the greater difference in a given month between the two years.*

3.4 Influence of external forcing factors on calving events frequency and wave height

Additional analyses have to be assessed to understand the reasons for the differences in the frequency and wave heights of the calving events in the data set. To know if something is behind such variations, analyses of external forcing factors are necessary. To do so, six external forcings have been compared to the calving activity and their respective wave height. Those factors are the quantity of ice mélange present in the fjord (divided into 4 categories, see section 2.4.2), the wind speed (m/s), the relative humidity (%), the air temperature (°C), the glacier flow variability (m/yr), and the tides.

3.4.1 Impact of ice mélange on calving activity

3.4.1.1 Impact on calving frequency

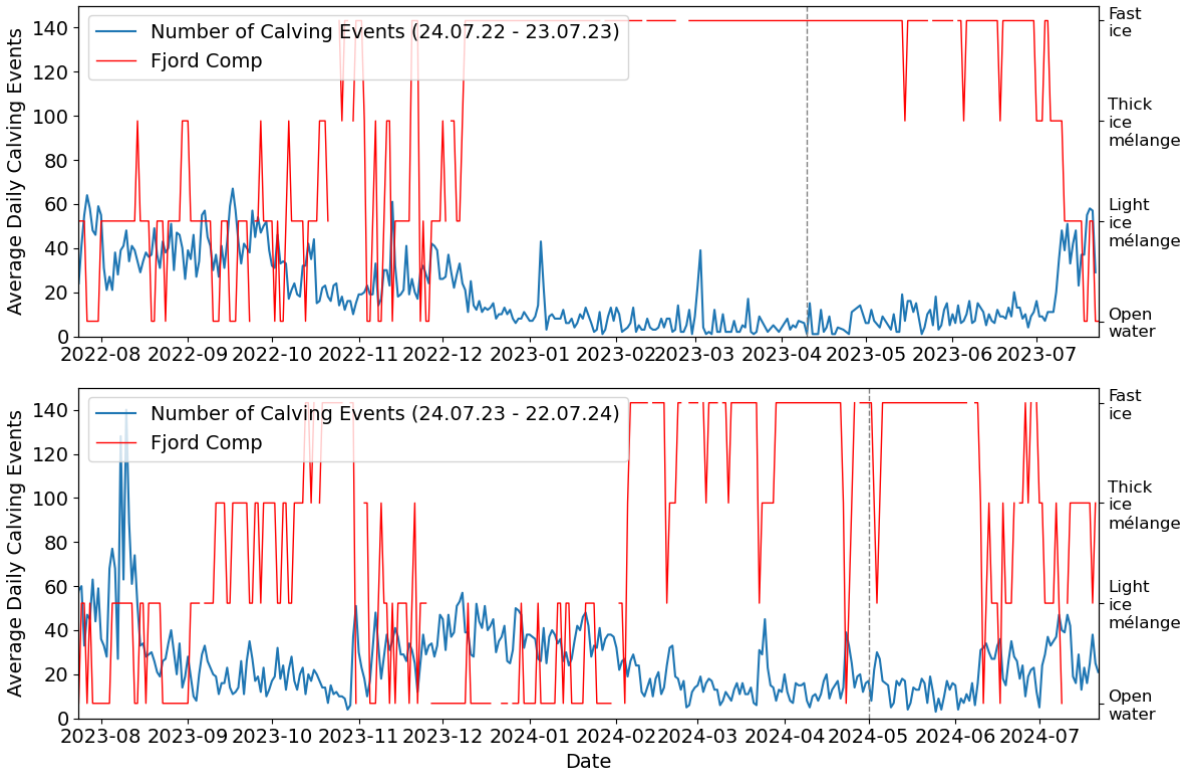

Figure 21: *Daily average number of calving events detected during the two years (08.2022 - 07.2023 and 08.2023 - 07.2024 in blue). The ice mélange quantity in red on both subplots is made of four categories: open water, light ice mélange, thick ice mélange, and fast ice. The grey dashed line represents the day when the fjord opened for the first time at the tide gauge location (see section 2.4.1).*

In figure 21 the comparison between the daily number of calving events (in blue) and the evolution of the quantity of ice mélange present in the fjord (in red) is represented. The figure is divided into two graphs, with the first year (August 2022 - July 2023) being on the graph on top, while the second year (August 2023 - July 2024) is below. The grey dashed line shows the day when the bay opens for the first time of the annual year (see section 2.4.1 for more information). Concerning the dashed line, no influence of the opening of the bay is visible. No direct changes in the frequency of calving events can be seen.
This graph illustrates a direct link between frequency and ice mélange. During the periods when the daily number of calving events is higher than the average (the average number of events detected throughout the dataset being 22.26), the thickness of the ice mélange present in the fjord decreases, staying between categories 3 to 1. This occurred during four periods, where a thin ice mélange layer and a higher daily calving rate were present: between August and mid-December 2022, between end-July and September 2023, between November 2023 and mid-February 2024, and between mid-June 2024 and the end of the data set (22nd July 2024). During the rest of the dataset, the daily calving frequency is lower than the average, with globally a higher ice mélange density

on the fjord, staying mostly in category 4, with some short periods in categories 3 and 2. This happened during three periods of time: first between December 2022 and June 2023 continuously, then between September and October 2023, and between February and May 2024. In the last section, four exceptions can be seen, with drops to category 2 and even one time until category 1, with complete open water.

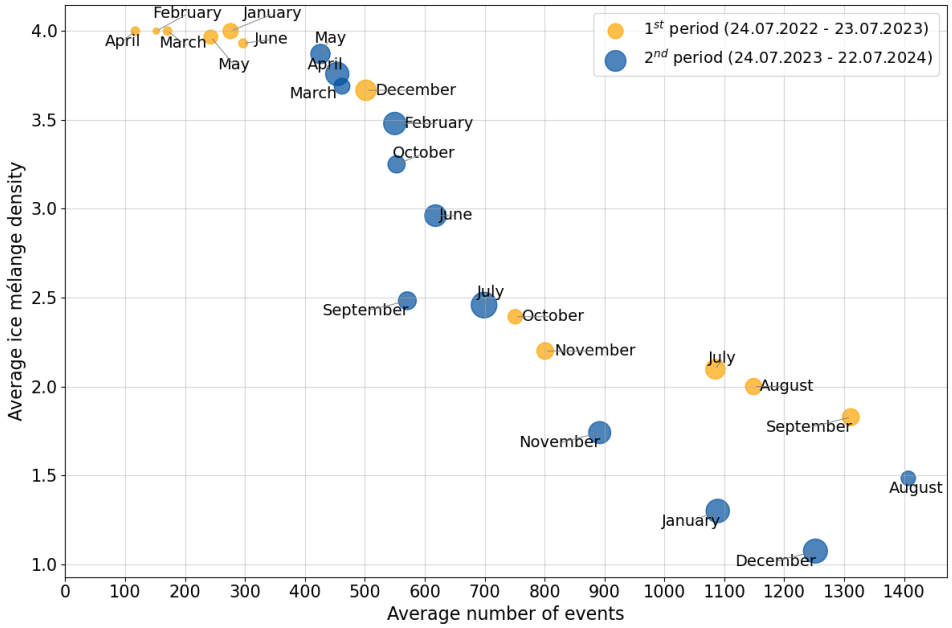

Figure 22: *Monthly average number of calving events compared to the average ice mélange density present on the fjord. The first year is in orange and the second in blue. Each month has a different point size depending on their median wave height over the month.*

To better understand how the amount of ice mélange in the fjord influences the frequency of calving, the figure 22 shows each month of the data set as a comparison between the frequency of calving activity and the categories of ice mélange. Each month has a circle size adjusted to the median wave height that occurred in each month. The first year is visible in orange, and the second year is visible in blue. The graph shows the number of calving events that occurred within a month on the x-axis, and the monthly average density of the ice mélange on the y-axis. A trend can be identified: the more events there are during a month, the thinner the density of the ice mélange (lower category). A spearman correlation with a value of -0.977 and a p-value of 2.505×10^{-16} shows a strongly significant negative relationship.
In more detail, the six months with the less calving activity are during the first year (in order: April, February, March, May, January, and June). These six months also have a smaller median than the one from the respective second yearly period. In addition, the month with the highest number of calving events recorded (August 2023) does not have a specifically high median size, suggesting that a lot of small events occurred. This aligns with the PDF representation from figure 17.

3.4.1.2 Impact on the wave height

The figure 23 illustrates the 20 biggest events detected within each of the four categories from the ice mélange database (see section 2.4.2). It has been chosen to use only the 20 largest events to better see the impact of the ice mélange on the big waves, to see how large waves can or cannot travel through a thick ice mélange. Using more events in this analysis would have lost its importance and its results. This graph is important to answer the question whether the ice mélange present in the fjord would smooth the waves and dampen the signal recorded by the tide gauges, especially during the winter and spring months.
What can be seen is that the range height of the 20 biggest waves in each category stays the same, with a maximum during a frozen fjord period. For this figure, the event detected on 13th July 2023 at 07:21:52 (with a wave height of 2.54 m) has been removed because of an unusual shape in the record. The tide gauge at this time was out of water half of the time when this event occurred, due to the combination of low tide and large waves. The differences in wave height between the frozen fjord, the light ice mélange and the open water categories are not significantly different, but the thick ice mélange category is statistically different compared to the light ice mélange and frozen fjord categories, with a p-value of 0.00019 and 0.0096 respectively, using the Mann-Whitney U test. The light ice mélange and open water categories are also statistically different with a p-value of 0.00104. If we merge the frozen fjord and thick ice mélange categories and compare them with the light ice mélange and the open water categories merged together, their difference is no longer statistically different (p-value 0.155). This graph suggests that there is no influence of the density of the ice mélange on the tide gauge records for large waves.

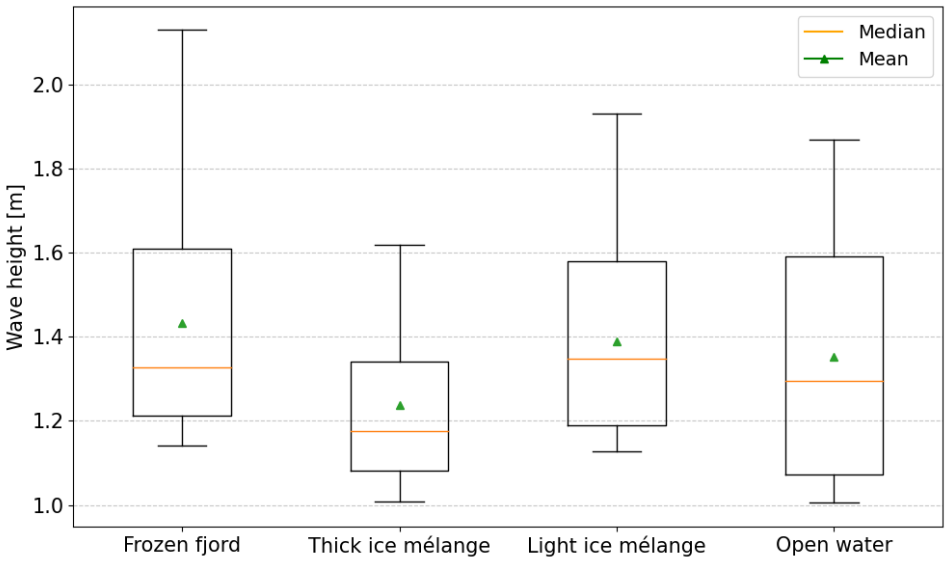

Figure 23: *20 biggest events detected occurring during each category of fjord sea-ice.*

3.4.2 Meteorological influence

3.4.2.1 Long time scale evolution using the Narsarsuaq dataset

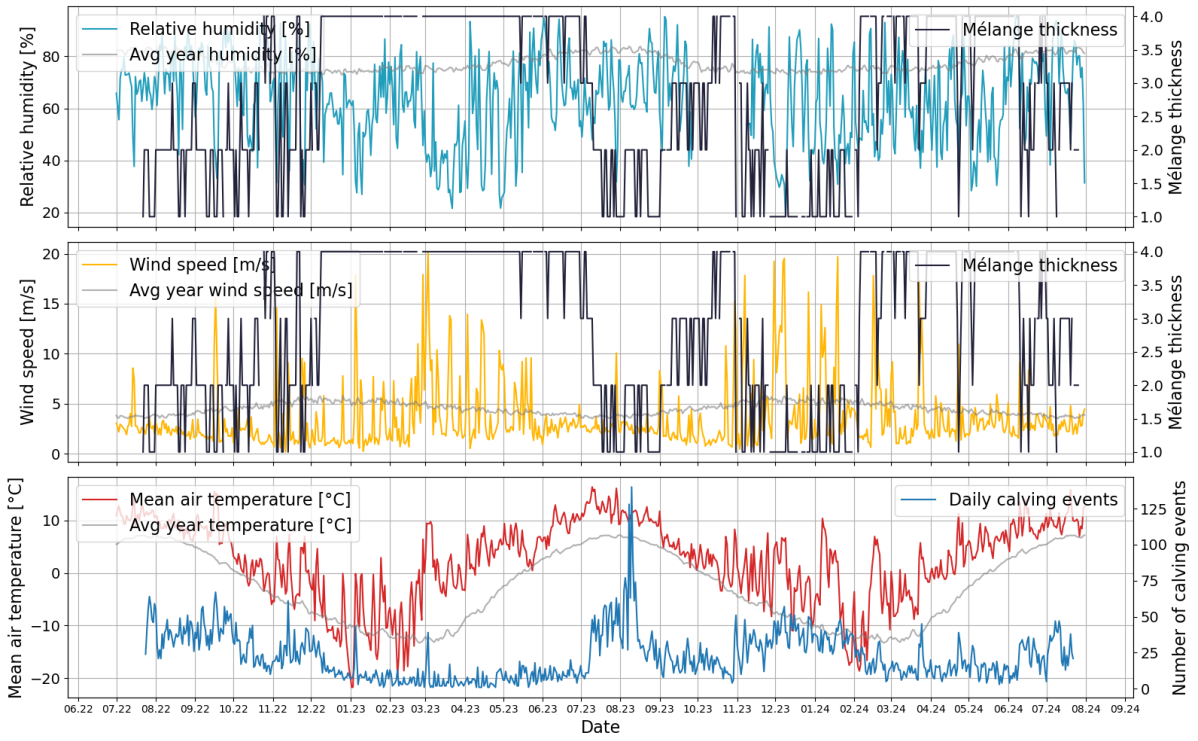

Figure 24: *The first graph shows the relative humidity (in light blue) and the second graph shows the wind speed (in yellow), both compared to the fjord composition (in black). The daily average temperature (in red) is shown in the third graph and compared to the number of calving events in blue. The three graphs show data from July 2022 to August 2024. The grey curve in each graph represents the average relative humidity, the average wind speed and the average temperature recorded between 1958 and 2023.*

Air temperature, wind speed, and relative humidity are three important factors that cannot be neglected when looking at external forcing factors. What is interesting is that foehn events, a high south wind combined with low relative humidity, can modify the quantity of ice mélange present in the fjord, as visible in the two first graphs in figure 24. Four short periods where the ice mélange curve drops from category 4 to category 2 or 1 can be visualised in figure 21 in section 3.4.1.1. Those events happened between February and May 2024 and are typical examples.
Figure 24 shows the relative humidity (%) in blue on the top graph, while the second graph right below shows the wind speed (m/s) in yellow. As data have been available since 1958, a grey line has been added to each of the three graphs to show the average relative humidity and wind speed over a period between 1958 and 2023. The time series represented in this graph extends from July 2022 to August 2024 (Publikationer Og Rapporter, s. d.). Both graphs have as a comparison the four categories of the ice mélange thickness evolution visible in black. This allows a better view of the changes of the ice mélange on the fjord with the respective foehn events. To find foehn events, a wind speed greater than 7.5 m/s and a 20 % drop in relative humidity or less than 50 % were chosen. A total of 47 foehn events have been found in the data set with the chosen parameters.

Figure 24 does not directly point out these events, but they can easily be seen each time the wind speed curve (yellow) increases sharply. To see if a foehn event breaks the ice mélange in most cases, we looked for a drop in the ice mélange density from two days before to two days after the 47 events. A total of 21 events remained. This difference has been tested as not significant considering the binomial test, with a p-value of 0.81, which means that foehn events do not significantly increase the likelihood of ice mélange break-up in most cases.
The influence of air temperature on calving activity is also an important external factor that can change calving variations. The last graph in figure 24 shows the number of calving events detected by the tide gauge P1 (in blue) and the daily average air temperature (°C) (in red). The grey line represents the average air temperature during the period from 1958 to 2023, the same period as for the wind speed and relative humidity. Concerning the temperature, it does follow the grey line shape, being a few degrees higher during the whole period, with the exception between November 2022 and February 2023. The variability in temperature is higher during this period. This behaviour is visible again, but with a lower range of variability between mid-October 2023 and March 2024. The highest peak of calving events detected in August 2023 occurred in summer, but abnormally high temperatures were not detected.
For example, at the start of January 2023 and March 2023, abnormally high temperatures correlate with a higher number of calving events detected. In addition, a drop in relative humidity and a high wind speed are also present. These are two typical examples of periods where three external factors together (relative humidity, wind speed, and air temperature) influence a fourth factor (the presence of ice mélange), leading to an increase in the number of calving events.

3.4.2.2 Temperature evolution in July 2024 compared to the daily number of calving events

Two weather stations were also deployed, one on top of a hill and the second near the shore (see section 2.3.3). The air temperature evolves differently depending on the two locations. Near the shore of the fjord, the temperature is usually colder than up a hill as a result of cold air coming down from the glacier. Figure 25 shows this different evolution during the two weeks of the field camp (12.07.2024 - 25.07.2024). The temperature near the shore (in orange) is colder than the one on top of the hill (in red), except on 20th July in the early afternoon. On this day, the temperature range for the entire day on the shore is 20 degrees, while on the hill it is only 8 degrees.
Compared to the daily number of calving events occurring during this period, no real trend can be found as those two weeks are in the same month of the same season, with constant sunny weather. The day with the highest number of calving events is July 12th, while the average temperature on the hill and on the shore is relatively cold. On the 20th July, while the air temperature is at its highest, the number of calving events also increases, which could suggest a trend if there was not the counterexample on July 12th.

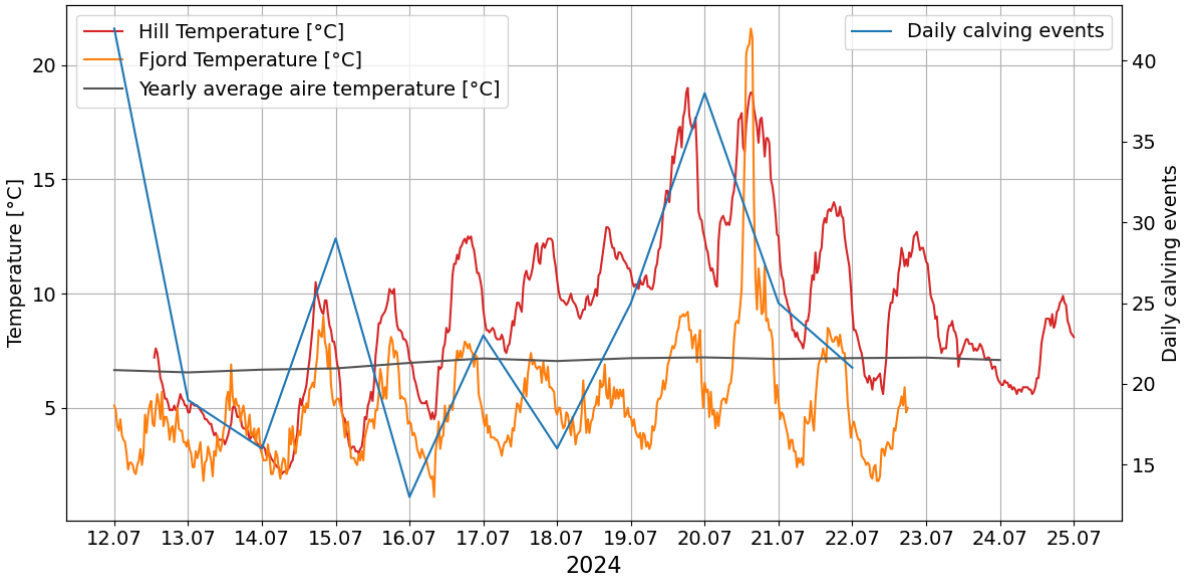

Figure 25: *Evolution of the air temperature at the hill (in red) and fjord (in orange) stations regarding to the daily number of calving events (in blue) that occurred on these days. The grey curve represents the average temperature recorded between 1958 and 2023.*

3.4.3 Impact of variations in ice velocity on the number of calving events

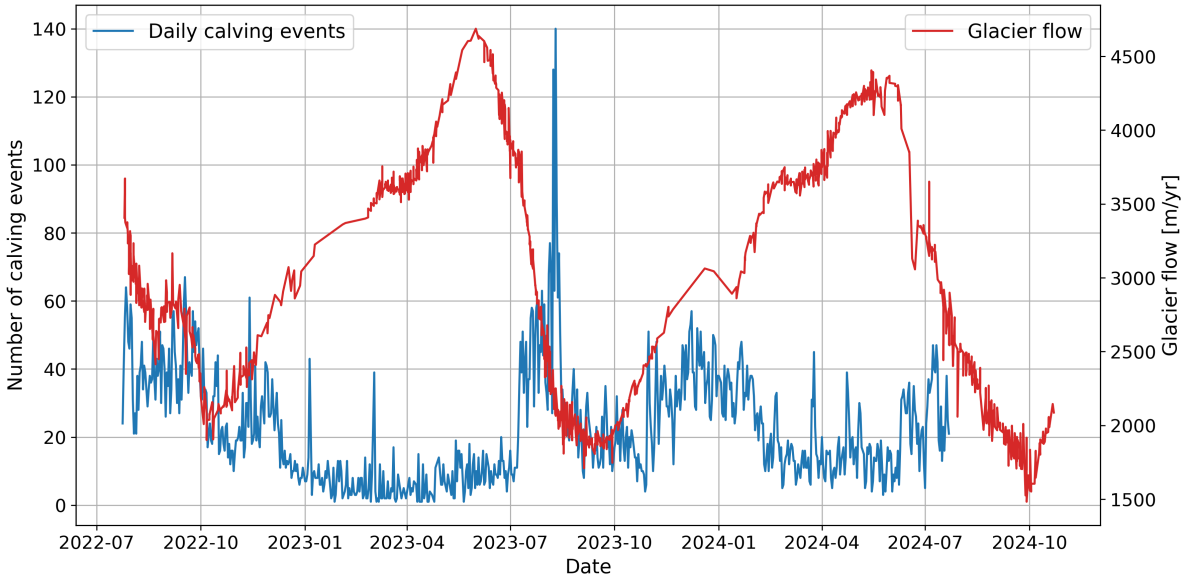

Figure 26: *Evolution of the glacier flow (in red) and the daily calving frequency (in blue) between the 24th July 2022 and the 5th October 2024.*

Figure 26 illustrates the EKaS glacier flow variability in red (its live a Nasa Measure Program, s. d.) and the daily number of calving events detected by the tide gauge P1 in blue over two years (between 24$^{\text{th}}$ July 2022 and 5$^{\text{th}}$ October 2024). The ice velocity varies in a range between 1'500 m/yr and 4'600 m/yr. This cycle is almost seasonal, with the lowest speed occurring in October, and the highest in June during both years.
Between 24$^{\text{th}}$ July 2022 and mid-November 2022, the glacier flow curve nicely follows the

evolution of the daily number of calving events: the lower it gets, the less calving activity. But after mid-November 2022, the blue curve decreases, while the red curve increases. In August 2023, the red and blue curves seemed to follow each other again until December 2023, before the blue curve decreases and the red curve increases again. No statistical correlation has been detected using Spearman correlation, with a coefficient of -0.03 and a p-value of 0.609.

3.4.4 Tidal evolution impact on the number of calving events

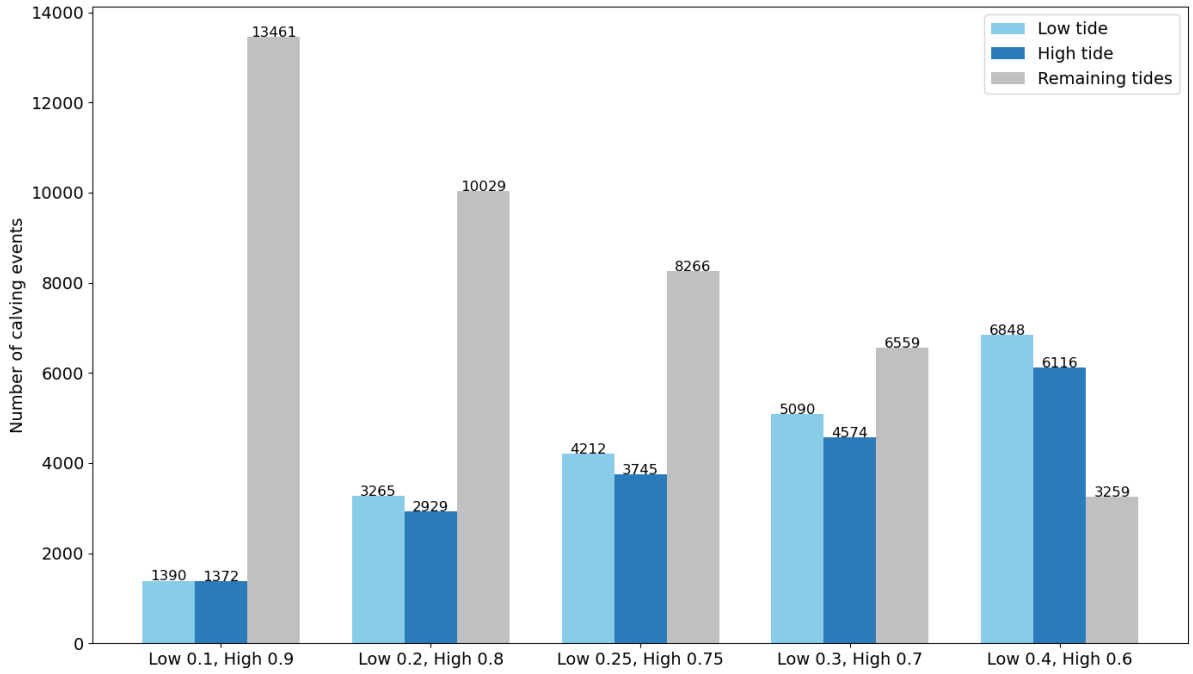

Figure 27: *Number of calving events detected above four different tide thresholds (0.9, 0.8, 0.7, 0.6) in dark blue, and below four different tide thresholds (0.1, 0.2, 0.3, 0.4) in light blue. The remaining events are visible in gray.*

Tides can influence the frequency of calving events. To understand the impact of tides on the number of calving events, a comparison between the number of calving events that occur during high tide and low tide has been made. Different simple thresholds have been used.

Firstly, a comparison was made between low and high tide. In figure 27, this comparison corresponds to the leftmost group of bars, labelled "Low 0.1, High 0.9", where the 10 % lowest and 10 % highest tide levels were used. The difference in the number of calving events detected between high and low tide is 18. The remaining calving events are plotted as a grey bar. Statistically, this difference is not significant using a chi-square test, with a p-value of 0.75. Additional comparisons have been made using other thresholds. The thresholds used are 20 % and 80 % for low and high tide, 25 % and 75 %, 30 % and 70 %, and 40 % and 60 %, respectively, shown in figure 27 as the next group of bars. The difference between low and high tide is, respectively, 336, 467, 516, and 732. Each of them is statistically significant using the chi-square test, with p-values being 0.000201, 1.79×10^{-5}, 7.16×10^{-5}, and 0.00021 respectively. Even with a statistical significance

and a visible trend to an increase in difference between low and high tide, it is normal, as the thresholds include more events. Therefore, this result should be taken with caution. In addition to these tests, it has been checked whether there was a significant difference in the number of calving events during rising and falling tides. Even if there was a slightly higher number of calving events occurring during a rising tide (3'891 events detected at rising tides and 3'591 events at falling tides over the two years of data set), these differences were not significantly different.

3.5 Comparison of the tide gauge detection and other detection methods

To improve the understanding of the tide gauge detection method, a comparison of the tide gauge data and three other detection methods is described in this section. The other detection methods are terrestrial radar interferometry (TRI), manual observations, and seismic records. Two of the three detection methods (TRI and manual observation) were used during data processing, which has been explained in section 2.4.3. Here we present how the three complementary methods are correlated with the tide gauge data.

3.5.1 TRI correspondence

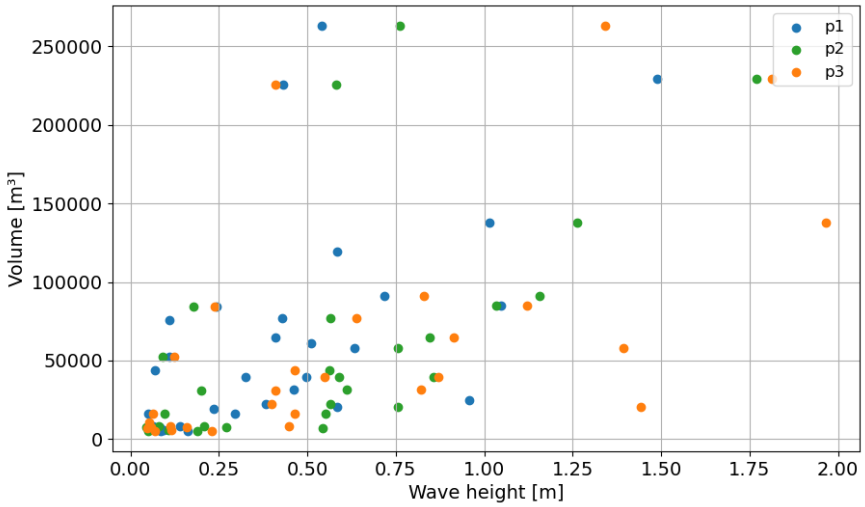

Figure 28: *Comparison between wave height and ice-fall volume, using the tide gauge and terrestrial radar interferometry (TRI) data. Each point is an event that have a value from one of the three tide gauges and the TRI records, with each tide gauge being illustrated with a different colour: blue for P1, green for P2 and orange for P3.*

The TRI method detected 31 events during the 7 days of record in July 2024. The goal is here to know if the 31 events detected by the TRI were also detected by the three tide gauges. To do so, a Python algorithm tried to find out if within an hour before or after a TRI event (this 1 hour time has been chosen due to the TRI time uncertainty and the tide gauge time uncertainty), an event was detected by each of the three tide gauges. In total, a correspondence of 30 calving events was found with P1, 28 with P2,

and 29 with P3. The figure 28 illustrates each event, with the height of the calving wave as the x-axis and the respective estimated volume from the TRI data as the y-axis. A trend can be identified: the larger the event is from the tide gauge data, the larger the volume is from the TRI data. A spearman correlation of 0.606 with a p-value of 0.001 was calculated, using events of P2 (green). This means that there is a statistically significant relation between the TRI and the tide gauge data.
In addition to the statistical correlation, some events can be defined as outsiders (2 events for P1, 2 events for P2, and 2 for P3). The first two events from the left that have a volume higher than 200'000 m^3 have a too high volume compared to their respective wave height. Those events do not align with the correlation, even if the three major green events from P2 in terms of volume are taken into account for the statistics.

3.5.2 Manual observations correspondence

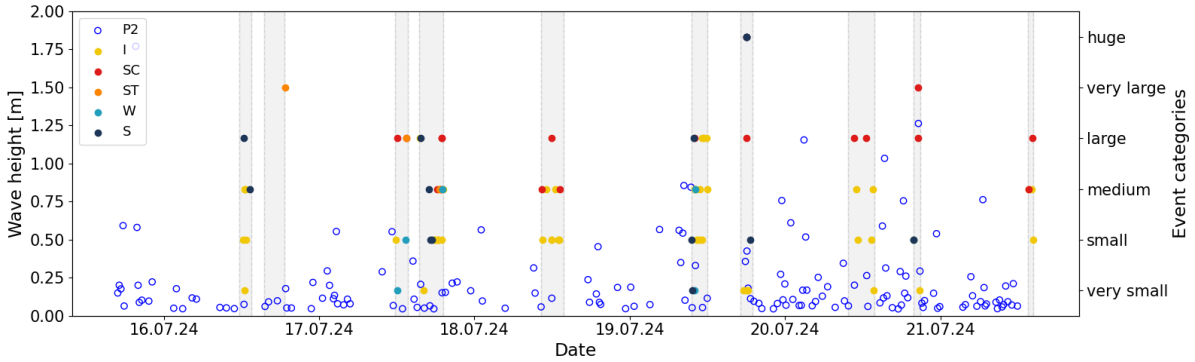

Figure 29: *Comparison between the manual observations made during the field camp (filled coloured points referring to the right y-axis) and the tide gauge P2 record (in blue, referring to the left y-axis). The light gray shaded rectangles refer to periods when manual observations were made. Each colour refers to a type of ice fall. The yellow points (I) are ice-fall events, the red points (SC) are sheet collapses, the orange points (ST) are stack topples, the light blue points (W) are waterline events, and the dark blue points (S) are subaqueous events.*

Figure 29 shows the ten periods in which manual observations were made, with, in colour, each observation that was described during the field camp with their associated type of fall (I, SC, ST, W and S). In general, the events manually described are spread over six very different size categories, while the possible corresponding events detected from the tide gauge are quite small compared to some other events that occurred over a time period without manual observations. The interesting aspect here is the invisibility of events categorised as "huge" on the tide gauge record, or only with a medium or even a small wave height. Only one event was described as "huge", as a subaqueous ice-fall type. Another interesting point is that for each of the 10 periods where manual observations were conducted, more calving events are described from manual observations compared to the number of calving events detected using the code algorithm.
Regarding the type of fall, the ice-fall calving type (I) is mostly present in lower-size categories, even if they are spread quite uniformly between "very small" and "large" events. The sheet collapse types (SC) are mostly bigger events, spread between "medium" and

"very large" size categories. Concerning the stack topples types (ST), only a few events have been categorised as such, with only one "large" and one "medium" event. The waterline types (W) are also present in a lower frequency, spread between the "very small" and "medium" categories. Lastly, subaqueous events (S) are spread over the entire range of sizes, making it difficult to extract any trend.

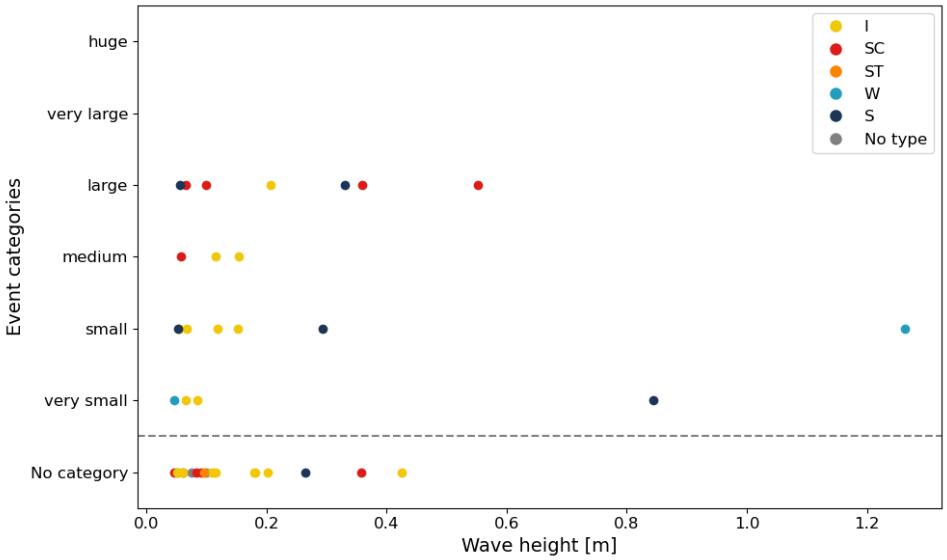

Figure 30: *Comparison between wave height and manual observations. Each point is an event that found a correspondence between the manual observations and the tide gauge P2 records. Each colour refers to a type of ice fall. The yellow points (I) are ice-fall events, the red points (SC) are sheet collapses, the orange points (ST) are stack topples, the light blue points (W) are waterline events, and the dark blue points (S) are subaqueous events.*

To test if a link between the manual observations and the tide gauge record emerges, the data have to be rearranged. Figure 30 illustrates the wave height extracted from the tide gauge as a x-axis, compared to the six categories of manual observations as a y-axis. Each point in this graph is an event that was detected by the tide gauge and a corresponding event from the manual observations, with 41 events in total. The way these two detection methods have been linked is by using an algorithm that finds an event with the closest time delay between the manual observation records and the tide gauge records, with a maximum of ten minutes due to tide gauge response delay. The type of fall that has been previously described is still visible with the same colours. Some events had no size categories assigned during the manual observations, which is why they are regrouped as the first rung of the y-axis, named "No category". Their type of fall and wave height are still visible. A Spearman test with a value of 0.178 and a p-value of 0.265 concludes that there is a non-statistical correlation between manual size categories and tide gauge wave height.

3.5.3 Seismic data correspondence

To see if a comparison between seismic data and tide gauge data is relevant, two periods were chosen. The first period is free of ice and the second period has a complete frozen fjord. Figure 31 shows the daily average wave height of calving events detected by the

tide gauge (in green) and the seismic data (in blue). The upper graph shows the period of time in which the fjord was free of ice (28th November to 8th December 2023) and the graph below shows the period with a complete frozen fjord (5th May to 5th June 2024). Speaking only of the ice-free period (upper graph), 13'957 events were detected by the seismic method (1'269 per day) and 467 by the tide gauge method (42 per day). During the frozen fjord period (lower graph), 39'289 events were detected by the seismic method (1'309 per day), while only 356 events were detected by the tide gauge method (12 per day).
Considering the seismic data, as "1/cf" (corner frequency) is an approximation of the calving event size, a comparison can be made (see section 2.3.4). Looking at the upper graph, an opposite evolution is visible: as the daily average size of calving events detected by the seismic method (in blue) increases, the average daily size of waves detected by the tide gauge (in green) decreases. This was not expected, as the thought was that the average size of the calving would be the same. In the graph below, with a frozen fjord, the average size evolves the same for both methods, until 14th May 2024. From that day on, an opposite evolution takes place until 21st May 2024. Then the seismic data do not change anymore until the end of the period, on 4th May 2024. Concerning tide gauge data, its daily average wave height changes over time.

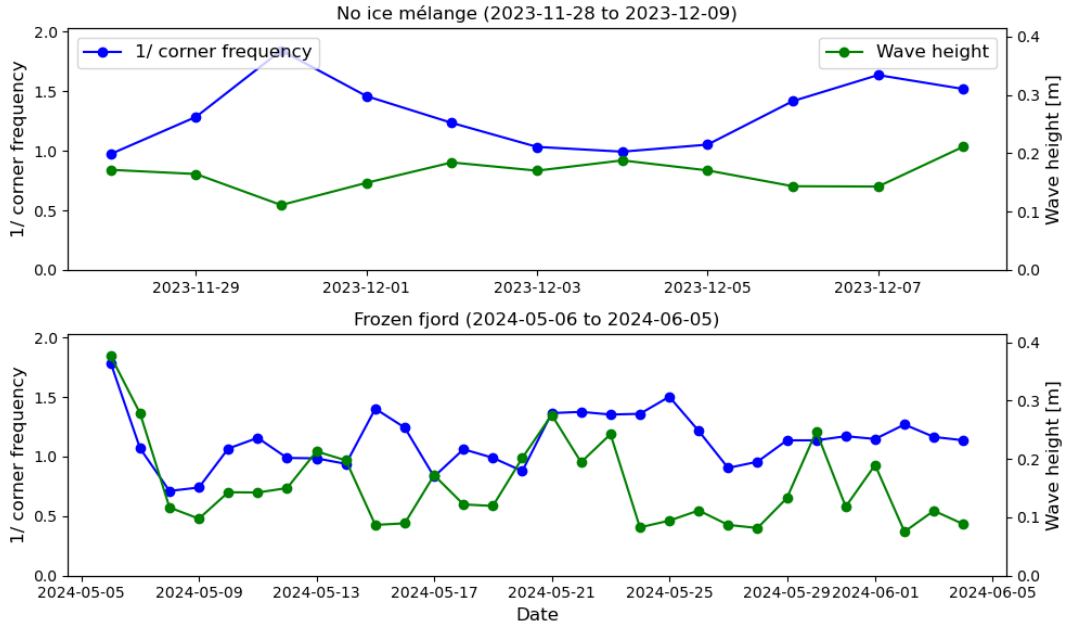

Figure 31: *Comparison between the average daily size (1/corner frequency) of calving events detected by the seismic method (in blue) and the average daily size of waves detected by the tide gauge (in green). The upper graph shows the comparison in the record with a fjord free of ice (28th November to 8th December 2023), and the graph below shows the comparison with a complete frozen fjord (5th May to 5th June 2024).*

4 Discussion

This study analyses the frequency and wave height distribution of calving events on the Eqalorutsit Kangilliit Sermiat (EKaS) glacier over two years (July 2022 - July 2024), using a tide gauge as the main instrument. To improve the understanding of the evolution and changes in the records, additional datasets were used, including records from three weather stations, four time-lapse cameras (figure 4), a database of thickness changes of the ice mélange (see section 2.4.2) and satellite images (figure 10). Further observations were made to compare tide gauge records and other detection methods, such as terrestrial radar interferometry (TRI), manual observations during the field, and seismic data.
The results show clear seasonal variations in the calving activity, with a significantly higher frequency of events during the summer months. This dynamic is correlated with a lower presence of ice mélange in the fjord, which may influence the detection. The temporal distribution of events was analysed at different scales, including seasonal, monthly, and daily variations (see sections 3.1 and 3.3). Additionally, wave height distributions were examined on both short and long time scales (see sections 3.2 and 3.3), allowing for comparisons over the full observation period as well as within individual months. The influence of external forcing factors, such as the thickness of the ice mélange, meteorological parameters (temperature, wind speed, and relative humidity), variations in glacier flow and tidal cycles, was also evaluated in relation to calving frequency and wave height (see section 3.4).
The discussion focusses on the four research questions exposed in section 1.4.1. First, an analysis of how the frequency and wave height distribution of calving events vary over the two-year observation period is performed. Then, it discusses how the location of a tide gauge changes its record response on a daily time scale. After that, a discussion of the influence of external factors, including the presence of sea ice (ice mélange), atmospheric conditions, glacier flow variability, and tides, is conducted on both the frequency and wave height of calving events. Finally, an evaluation of suitability of a tide gauge to be used alone to monitor calving activity is assessed, taking into account the challenges to extract calving signals, for example when the ice mélange is thick and can alter the signal.

4.1 Interpretation of results

4.1.1 Relation between wave height and frequency of calving events

Analysis of calving events over a two-year period showed significant variability in both the frequency distribution and the size variability of the wave heights, with a strong seasonal influence. Although the number of events fluctuates significantly throughout the data set, the median wave height remains constant over time (figure 19). One reason for this may be because the glacier is highly crevassed, which increases the ratio of smaller events with a higher frequency, as illustrated by the PDF method (figure 17). This aligns with previous studies suggesting that highly damaged ice leads to frequent but smaller-scale calving events (Kneib-Walter et al., 2023). In contrast, large-scale calving events, even if they are less frequent, contribute disproportionately to total ice loss (Jouvet et al., 2017; Enderlin et al., 2014). This can explain why some periods still have a higher median wave height, such as, for example, in March 2023 (figure 19).
A key observation is the monthly and seasonal variability in calving frequency (figures

13 and 14). The summer months appear to be the period with the highest number of events occurring (July and August), with the possibility that this high number of events extends to September. This is the case only in the second year of the data set (September 2023), as it depends on when the cold period starts. In contrast, the winter and spring months appear to be the periods with less calving activity (December to June). The presence of ice mélange appears to be the main controlling factor. The ice mélange, when densely packed, acts as an inhibitor of calving (Wehrlé et al., 2023), mainly for small events (figure 19). This is particularly evident in the winter and spring months, when the fjord freezes until it creates a thick ice mélange that can considerably reduce calving activity (see section 2.4.2 with the four ice mélange thickness categories). However, external forcing, such as atmospheric conditions, can alter this balance. A contrast is observed between December and January of the two years studied (figures 14, 20 and 22). In the first year, a fully frozen fjord was present in the fjord with low calving activity recorded, while in the second year strong foehn winds coming from the ice sheet broke the ice mélange, which dispersed the ice blocks further down the fjord (figure 24). As a result, the number of recorded calving events was significantly higher. Vieli and Nick (2011) found that reductions in winter ice mélange thickness and duration can drive to a rapid glacier retreat, which could be translated to our case to add another point to the findings: less ice mélange present on the fjord over a season increases the average number of calving events occurring daily over a year, which consequently makes the glacier front retreat. Concerning the EKaS glacier itself, the glacier front does not retreat for now, as can be seen in figure 5. This is supported by Nick et al. (2009) by the fact that tidewater outlet glaciers adjust extremely rapidly to changing boundary conditions at the calving terminus. So, the frequency of calving events is highly influenced by the presence of ice mélange, how crevassed the glacier is, the time of year when the cold temperature arrives and the foehn events that change the quantity of ice mélange present on the fjord.
Beyond the seasonal scale, the variability in calving activity is also influenced by several environmental factors and the physics of the ice fall. The type of ice fall (submarine event, cliff collapse, or buoyancy-driven event) plays a role in influencing the magnitude of the wave of individual events (Benn et al., 2007; Heller et al., 2019), which is why two same volumes of ice that fall into the fjord will not have the same wave height on the tide gauge record (figure 30). Variability in the way ice falls into the fjord cannot explain variations over long time scales but can explain daily fluctuations in terms of wave height detection, especially when using average wave height over certain time scales. For example, the average wave height present on figure 19 illustrates perfectly this problematic: the 10th March 2023 was recorded only two important events using the algorithm which increased the daily average wave height significantly.
Additionally, air temperature fluctuations contribute to diurnal and seasonal calving frequency variability. Increased melting and subglacial discharge can lead to short-term peaks in calving activity (Dachauer et al., 2024). The relationship between ice velocity and calving also supports the observation that the more calving activity occurs at the glacier centre, where the subglacial freshwater plumes emerge.

4.1.2 Tide gauge location variability

The analysis of tide gauge responses on a daily time scale shows significant variability depending on their location. During the one-week period when all three sensors were

installed, clear differences emerged between the P1, P2, and P3 records.
The first tide gauge (P1), located on the same side as the glacier front about 1.5 km east, recorded significantly fewer events than P2 and P3 (figure 15). The events detected by P1 were generally of smaller magnitude (figure 18), leading to a smoother signal with less pronounced peaks. Its distance from the calving front has an effect on the "sharpness" of the peak as a wave travelling on a longer distance is reduced in height and the wave becomes longer (Minowa et al., 2019). The placement of P1 behind a stable rock (see figure 6) filters and modify the waves and their height. The topography of the fjord also affects the signal as the fjord around the P1 location is much more shallow than just in front of the glacier. In contrast, P2 and P3 were installed on the opposite shore of the glacier with direct exposition to calving waves. The records were therefore more distinct, and it was easier for the algorithm to detect events. Between P2 and P3, P3 showed even more peaks (see table 3), which can be attributed to both its local placement and the conditions of its mounting (Rabinovich, 1995). As for P1, P2 was placed behind a big rock near the shore, which can have the same effect than previously explained for P1. Unlike P1 and P2, P3 was fixed to a loose metal cable laid on the sea floor. Even if a rock was attached to it to keep it from moving, this setup likely introduced additional movement in response to waves and tides, possibly amplifying certain signal components while also introducing noise. Unfortunately, this effect is not measurable.
Statistical analysis of event-detection differences further illustrates the discrepancies between the three tide gauges. When considering events detected by both P1 and P2, 106 events were identified, with 11 false detections (a peak that was detected by the algorithm but should not be counted as a real event) and 13 missed events (an event that was very similar to a calving wave, but was not counted by the algorithm), as visible in table 2. In addition to the one detected from both tide gauges, P1 detected 34 more events that P2 did not detect, but falsely detected 24 events that were not real events and missed 15 real events. In comparison, P2 detected 56 more events in addition to the 106 detected by both sensors, with only 8 more false detections and 2 more missed events, reinforcing its better response to wave activity. In total, P1 falsely detected 35 events and missed 28 events, while P2 falsely detected 19 events and missed 15 events. With a p-value of 0.0062, a significant difference is calculated. This shows how the location of the tide gauge is important and can change the results we get.

Sensor	Nbr detected	False detection	Missed events
P1 + P2	106	11	13
Only P1	34	24	15
Only P2	56	8	2
Total P1	140	35	28
Total P2	162	19	15

Table 2: *Number of events detected with both pressure sensors (P1 and P2) or only one of them.*

The trend continues when comparing P2 and P3 (table 3). Both detected 140 events, P3 identified 36 additional events beyond those captured by both and P2 22 more events that P3 did not. However, both sensors exhibited 19 false detections in total and P3 had slightly more missed events (16 compared to 15 for P2). Using a chi-square test, a p-value of 0.97 was found. The difference between the two sensors P2 and P3 records is

therefore not significant. Their signal is close, with a better detection than that of P1. Overall, it results in 103 events detected from all three sensors with 7 false detections and 7 missed events (table 4). This highlights the fact that all three sensors detected only 58 % of all events detected from P3, suggesting that this method could and should be further developed.

Sensor	Nbr detected	False detection	Missed events
P2 + P3	140	10	13
Only P2	22	9	2
Only P3	36	9	3
Total P2	162	19	15
Total P3	176	19	16

Table 3: *Number of events detected with both pressure sensors (P2 and P3) or only one of them.*

Sensor	Nbr detected	False detection	Missed events
P1 + P2 + P3	103	7	7

Table 4: *Number of events detected with all three sensors.*

An important factor influencing the detection accuracy is the shape of the recorded signals. As calving waves propagate through the fjord, their intensity and distinctness vary depending on the location of the sensor and environmental factors (Minowa et al., 2019). The smoother record at P1, with less distinct peaks, made it more challenging for the algorithm to identify calving events (Kneib-Walter et al., 2021). The flatter and longer wave signal shape led to a higher likelihood of miss events, as seen in the P1 record. Another way to miss often an event is when a small event occurs just before a larger one. This was visible in the three sensor records and illustrated in figure 32 with a short period of the tide gauge record P2. Conversely, false detections were often triggered by the decay phase of a large wave, where the gradual decrease in signal amplitude made the algorithm think that secondary event peaks were occurring. P2 and P3, with their clearer and more intense wave responses, exhibited fewer detection errors. Therefore, the observed differences between P1, P2, and P3 may be partially explained by the fact that the near-shore tsunami records are strongly influenced by local topographic effects (Minowa et al., 2018). All this is visible in both figures 15 and 18. In the first figure, fewer calving events are detected at the P1 location, compared to P2 and P3. In the second graph, these behaviours are represented by the

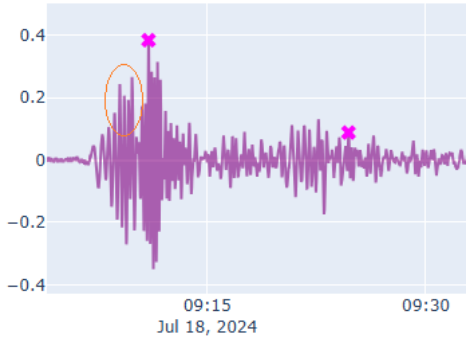

Figure 32: *Snapshot of a tide gauge record. The purple crosses are the peaks detected by the algorithm. Just before the first cross, we can see visually another calving event that was not detected by the algorithm surrounded by an orange circle.*

fact that the three biggest events are detected by the P2 and P3 sensors and that P1 detected more small events than the other two sensors. The longer a wave needs to travel to arrive at the P1 location, the more the wave will be attenuated (Minowa et al., 2019). The implications of these variations in the response of the tide gauge extend to the broader interpretation of calving activity. A more distinct wave record, such as those captured by P2 and P3, allows for a more accurate identification of events, reducing uncertainties in event frequency and size estimates over a longer time scale period. This means that fewer detections using P1 do impact the number of calving events detected over the two-year period, which ultimately underestimates the calving activity. Placing the tide gauge directly in front of the glacier is a better option, even if P1 was placed on the side of the glacier to limit the pressure exerted by the ice mélange during the winter and spring months. Furthermore, while P3 recorded the highest number of events, the potential influence of its loose mounting must be considered, as it could contribute to add noise to the record. In addition, it is important to look at the local topography in detail before installing a tide gauge to limit this effect on the record.

4.1.3 External forcing factors in relation with wave height variability and frequency of calving events

In this section is discussed how external forcing factors, such as the presence of sea ice (ice mélange), atmospheric conditions, glacier flow variability, and tides influence the variability of wave height and the frequency of calving events.
The ice mélange and the accumulation of calved icebergs in front of the glacier terminus play a significant role in modulating calving activity, as suggests in figure 21. Observations indicate that dense, packed ice mélange acts as a damping agent, suppressing or reducing the detection of calving, especially for small events (figure 23). The bigger waves can still travel through the fjord as they have more energy to move the ice. For instance, Wehrlé et al. (2023) demonstrated that the presence of a dense ice mélange effectively inhibits calving on a short time scale. Similarly, Kneib-Walter et al. (2021) observed a notable increase in calving activity at the start of the melt season, coinciding with the thinning of ice mélange layer. This suggests that the mechanical support provided by the ice mélange stabilises the glacier terminus, and its absence increases the occurrence of calving. Further supporting this, Bartholomaus et al. (2015) reported elevated iceberg calving flux during summer and fall, with a marked reduction in mid-winter, which matches with the seasonal presence of ice mélange. Cassotto et al. (2015) also found that freezing of the ice mélange during winter leads to decreased mobility of the mélange, which is associated with a drastic reduction in iceberg production. To correlate with these studies, figure 22 shows a correlation between the number of events that occurred during a certain month and the average thickness of the ice mélange. This statistically negative relation explains once more the impact of the presence of ice mélange and the frequency of calving events.
Air temperature, relative humidity, and wind patterns indirectly influence calving activity by affecting the stability and presence of ice mélange. During the two years of measurements, episodes of foehn winds have been linked to the breakdown of the ice mélange (see figure 24). These warm south-orientated winds coming from the ice sheet associated with low relative humidity contribute to mechanically clear the ice from the fjord, thereby removing the dampening effect. This effect is significantly more visible

during the winter and spring months as the fjord is usually frozen. This is especially the case for the second year of the data set, as several foehn events occurred in December 2023 and January 2024, completely modifying the dynamics of these two months (see figures 14, 16, 20, 22). Minowa et al. (2019) reported higher calving rates during periods with elevated air temperatures and falling tides, suggesting that atmospheric warm winds contribute to mélange destabilisation. However, on an hourly time scale, the direct correlations between atmospheric conditions and the frequency of calving are less pronounced (figure 25). In this figure can be seen a difference in the maximum range of temperature change during an individual day. In July 20^{th}, the temperature range was 20 degrees, while on the hill it was only 8 degrees. This can be due to strong warm wind during the day, before the cold weather takes place again when the sun goes down. The only other relation on a daily basis is a four-hour delay between the highest temperature of the day and the highest frequency of calving activity (Dachauer et al., 2024).
Concerning the variation in glacier flow, it only partially follows the variations in calving frequency (figure 26). The glacier had a high velocity in late spring and a low velocity in autumn of both years, almost the opposite for the calving frequency, which had a low number of daily events in spring and a high number of calving events in summer. To support this point, no statistical correlation was found between the two curves in figure 26. The variations in glacier velocity are complex and as it cannot be directly linked to calving frequency, the changes of calving event rates over time are less influenced by this process than others, such as ice mélange coverage (Sugiyama et al., 2025; Vieli et al., 2001).
Tidal cycles were found to have a statistically significant influence on calving frequency if simple thresholds were used above the top 20 % and below the first 20 % in tide height. Specifically, a higher number of calving events are recorded during low tide periods. This pattern may be attributed to the reduction in hydrostatic pressure at the glacier terminus during low tides, which could facilitate fracturing and calving. Minowa et al. (2019) explained that an increase in calving rates is associated with falling tides, aligning with the observations in figure 27. However, the magnitude of this effect is relatively modest and, while statistically significant, does not represent a dominant control on calving activity.
Although external factors significantly influence the frequency of calving events whether on a daily, monthly, or seasonal basis, their impact on the wave sizes of individual calving events is less clear. No measurements on the influence of external forcing factors on the height of the calving wave were possible, except with the thickness of the ice mélange (see figure 23). Here, no statistical evidence of any impact on the calving wave height has been detected, which is a counterexample to the previous explanation of the ice mélange dampening the signal of the waves. An explanation for this discrepancy between the damping effect and this figure comes with the seismic detection method (figure 31). This method does not see any difference in terms of the numbers of calving events occurring with either a thick ice mélange or a fjord free of any ice. This is explained by the fact that the biggest waves produced by large calving events have enough energy to travel through the ice even in the presence of ice mélange. Only the smallest waves produced by small calving events are then dampened by the ice, which explains why in figure 23 it cannot be seen any statistical difference between the four categories of ice mélange. Only the 20 largest events were used to produce this graph. Ultimately, fewer calving events in terms of frequency give the same average daily wave height, which offset each other.

4.1.4 A tide gauge to monitor calving events?

This section discusses the question whether a tide gauge is sufficient to monitor calving events. Several studies have shown that a tide gauge can provide valuable information by capturing wave signals associated with ice fall (Kneib-Walter et al., 2021; Minowa et al., 2018). Minowa et al. (2019) found that calving events produce a distinct waveform that can be differentiated from other environmental signals, such as wind waves, tidal currents, or boats.

As an advantage, a tide gauge is a simple, inexpensive, autonomous, and long-lasting sensor. Studies have found the utility of such a simple sensor for measuring calving events, as the amplitude of surface waves increased with the size of the calving event (Minowa et al., 2019). This means that tide gauge data can provide an indirect measure of calving flux and event magnitude over a long period.

Despite these advantages, a tide gauge alone has limitations that restrict their ability to fully characterise calving events. One major challenge is the difficulty for one single tide gauge in locating precisely individual calving events along the glacier front. Minowa et al. (2019) emphasised that wave height measurements alone do not provide sufficient information to determine the exact location of an event. Waves are influenced by multiple factors, including bathymetry and ice mélange conditions. In addition, Minowa et al. (2018) explained that different types of calving produce similar wave spectra, making it difficult to differentiate between a high ice fall, a submarine calving, or a rotational collapse, even if some differences are visible on the records. In particular, Heller et al. (2019) showed that a submarine collapse has a peak wave smoother than an ice fall in the tide gauge record. The presence of ice mélange in the fjord does not help to detect calving events, as waves can be dampened depending on the energy of a wave produced by a fall (Amundson et al., 2010; Bartholomaus et al., 2015). In this case, big events are still visible as they have the power to travel even with a thick ice mélange, and small events are not visible in the tide gauge record. The fjord depth variations also significantly influence the shape of the waves in a tide gauge record (Minowa et al., 2018). This is particularly noticeable when comparing data from different tide gauge locations (tables 2, 3, and 4), which showed significant differences in their record. Here, the three tide gauges (P1, P2, and P3) were installed in areas with different bathymetric characteristics. This could contribute to the variability of the signal. P1 was located further east in the fjord in a shallow area, while P2 and P3 were installed in a deeper section of the fjord. However, the differences between P2 and P3, even if installed close to each other, suggest that the positioning of the sensor or the presence of a large rock next to it influence the records too.

With all this said, we can now say that tide gauges can efficiently monitor general calving trends over long timescales, but it is still hard to provide detailed information about individual events. We certainly do have information on the height of a wave produced by an ice fall, but it is hard to say exactly how large the volume of the ice that fell. Kneib-Walter et al. (2021) wrote that it is important to combine multiple observation techniques to overcome individual limitations and gain a more comprehensive understanding of calving processes. Integrating tide gauge data with time-lapse imagery, terrestrial radar interferometry (TRI) (Kneib-Walter et al., 2021 and 2023), and seismic records Walter et al., 2020; Amundson et al., 2010) as it has been done in this thesis provides useful complementary information to characterise calving styles, sizes and frequency.

To summarise, tide gauges provide a useful tool for monitoring calving activity, particu-

larly for identifying trends in calving frequency over a long time period and to characterise large events. A correction of the thickness of the ice mélange could be added to the detection algorithm to improve the precision of the detection method, as a statistical trend could be identified (see figure 22). However, the use of this method is insufficient for accurately measuring the loss of ice, mainly due to the sensitivity of the location of the tide gauge and the thickness of the ice mélange. Tide gauges can serve as a valuable component of a general monitoring framework, but if precise information about individual calving events is needed, integrating them with other observational methods is necessary.

4.2 Strengths and limitations

This thesis presents several strengths that improve the reliability of the analyses. The high temporal resolution of the wave height measurements provides a precise description of wave evolution over time, ensuring a detailed record of calving wave signals. In addition, no measurement issues occurred during the two years of sampling, which proves that long-term analysis is possible even without the need for constant monitoring. The methodology employed, an algorithm that extracts calving events created with a Python code, is also a strength, as it allows for the detection of a large number of events using a relatively simple approach based on a few variables only. Multiple independent measurement methods, including terrestrial radar interferometry (TRI), seismic data, manual observations, and time-lapse cameras, were also integrated into the study. These multiple sensors provided a cross-validation between different detection techniques that increased the understanding of the results. Finally, the fact that we assume that the four categories of ice mélange were present during the seven days used to choose the final thresholds makes the event detection process even more interesting and computationally efficient. The event extraction procedure was simplified as it was not necessary to add a variable or a correction for the ice mélange thickness category, allowing for a rapid analysis of calving activity over the two years of the dataset.
Despite these strengths, a number of limitations need to be discussed. A first issue concerns sensor placement, particularly for the P1 tide gauge, which had a smoother record shape. This made it harder for the code to extract the calving events. This is a major problem because the P1 record is at the heart of this thesis. A satisfactory number of events were extracted, but an improvement can be made to accurately determine the number of calving events that occurred over the two years of the dataset. Furthermore, while the correlation between the tide gauge data and the TRI detections was strong (figure 28), the presence of outlier events raised uncertainties regarding their interpretation. Outliers may correspond to specific types of calving events, such as submarine calving or rotational collapses. Manual observation showed that certain types of ice fall have a large range of calving volume (from "very small" to "huge" as a description), and others are limited to small or large events (figure 29 and 30). This may be one explanation for the outliers, but it does not explain it completely, as other factors such as the presence of ice mélange can change the wave height detected by the tide gauge. Another limitation is the long-term reliability of the event detection model. Although the method effectively captures trends in calving activity (seasonal or monthly evolution), it is not possible to systematically verify that each detected event corresponds to an actual calving occurrence. Tables 2, 3, and 4 show how different the response is between the three tide gauges and that a significant number of events were actually missed or falsely counted on

the seven days of records in which the three tide gauges were recorded at the same time. This raises the question whether the number of events detected over two entire years is really correct or not. This means that the results are more indicative of general trends rather than precise event-by-event validation.
The assumptions made regarding the thickness categories of the ice mélange also introduce potential sources of error. While this database is a very efficient way to categorise the two years, it may on the other side make miss long-term trends, particularly in periods with persistent thick ice mélange or complete absence of mélange. This problematic could be improved by creating a new part in the code that could correct the thickness of the ice mélange to reduce detection errors by artificially increasing the intensity of the signal. This could then remove the problem of a dampening effect and show more realistically the number of calving events occurring during winter and spring. Finally, even if a sensitivity analysis was performed to identify an optimal range of thresholds to balance false detections and missed events, the thresholds chosen can be questioned. If the thresholds are set too low, the model may detect some false events, but if the threshold is set to high, it may lead to missed detections of smaller events (see figure 12). Other studies found on other glaciers significantly higher number of calving events, which may question whether the thresholds should have been set lower to detect more smaller events (Kneib-Walter et al., 2021; Minowa et al., 2018).

4.3 Future researches and recommendations

Several methodological improvements could provide better detection and characterisation of calving events. Applying Fourier transform analysis (Ryo et al., 2016) could reveal how calving signals are distributed across different frequencies, with the potential to find influences that were not initially detected. Although tidal frequencies were removed from the tide gauge record (Kneib-Walter et al., 2021), other periodic signals may still be present and could be identified through this approach. Furthermore, a more precise localisation of calving events could be achieved by using the three tide gauges placed at different locations. With these tide gauges, it provides an opportunity for triangulation. This would be helpful to know how far a certain event is from the tide gauge location, to further improve the knowledge about the size of an event. A large event occurring further away from the sensor will have a smaller wave height recorded (Minowa et al., 2019), which can lead to errors when analysing the wave height distribution over several days. One can then create a correction of the wave height depending on the distance between an event and the sensor to have a more precise analysis. By comparing these observations with seismic data, the spatial accuracy could be further improved. Lastly, the use of ultrasound as a complementary indicator of calving activity is another method that could be further tested, given that calving generates both airborne and underwater acoustic signals (Marchetti et al., 2021).
Extending the observation period over additional years would provide a better understanding of long-term trends, particularly in relation to climate change. Some interesting questions are whether calving activity during summer months increases each year and if periods of high ice mélange coverage shorten due to warming changes in fjord and glacier conditions. Investigating these trends at seasonal and interannual scales could improve our understanding of how glacier-ocean interactions will evolve under changing climate conditions.

The integration of additional parameters, such as the role of seiches in modulating calving activity can help improving the code to better extract the number of calving using a tide gauge record (MacAyeal et al., 2012).
Calving plays a significant role in the ice loss of the Greenland Ice Sheet (GrIS), with approximately half of its mass loss attributed to the discharge of icebergs (Enderlin et al., 2014). As highlighted by Catania et al. (2020), more research is needed to improve long-term observations at the ice-ocean and ice-bed boundaries, develop better numerical models constrained by observational data, and encourage interdisciplinary collaboration. Beyond its implications for sea level rise, glacier ice loss also affects oceanic processes. The input of freshwater from calving events reduces the salinity of the fjords, estimates suggesting that 1 to 2 % of the water mass in these regions originates from glacial meltwater (Mortensen et al., 2013). This dilution effect can disrupt local ocean circulation and, on a larger scale, contribute to the weakening of thermohaline circulation (Grosfeld et al., 2001), an important driver of global climate regulation.

5 Conclusion

This study focused on the calving activity in Eqalorutsit Kangilliit Sermiat (EKaS) for a two-year period from July 2022 to July 2024 using tide gauge data as the primary detection method. In addition, multiple environmental variables were used, such as atmospheric conditions, tidal variations, glacier flow velocity, and ice mélange conditions. Terrestrial radar interferometry (TRI), satellite imagery, seismic signals, and manual observations were combined to cross-validate tide gauge records. The resulting calving event database was based primarily on wave height detection through a Python code. All of this was analysed to answer four main research questions concerning the frequency and wave height of calving events, the spatial variability in wave responses depending on the location of the tide gauge, external forcing influences, and the methodological reliability of the tide gauge to monitor calving activity.

The frequency and wave height distribution of calving events varied over the two years of record. The initial hypothesis predicted a strong seasonal signal, with a more frequent wave height occurring during the warmer months and a higher number of small calving events throughout the data set. This was confirmed by the data, where a seasonal and monthly pattern can be identified: a significantly higher number of calving events were recorded during the summer months (in July and August of both years, and in September 2023), and less events in winter and spring. However, exceptions were found in December 2023 and January 2024, where the frequency remained high, due to a lower ice mélange coverage, and several foehn events. In terms of the wave height distribution, a higher frequency of small waves was observed. The average wave height remained constant throughout the study period, although the second year recorded higher values on average. The overall distribution is in line with expectations, where small events are more frequent, while large events remain rare.

Then, it was analysed how tide gauge records vary depending on their location. The hypothesis assumed that the geometry of the fjords, the bathymetry and the boulders in the immediate surroundings would influence the reception of the signal. The results confirmed this, with the P1 tide gauge detecting 18 % less events than P2 and P3 on average. P1 also recorded flatter and lower-amplitude waveforms, which contributed to a higher rate of missed events and false detections. In contrast, P2 and P3, installed on the opposite side of the fjord and in close proximity, produced more consistent and comparable records, with P3 detecting 8 % more events than P2. These differences illustrate the influence of local topography and gauge location on wave propagation and detectability.

Subsequently, the impact of external forcing factors on calving activity, such as the presence of sea ice, atmospheric conditions, glacier flow, and tides, was assessed. The hypothesis suggested that if air temperature and wind are not likely to have a direct influence, the presence of ice mélange dampens wave signals and reduces detectability. This hypothesis was strongly supported by the data, as the ice mélange was shown to significantly dampen the smaller wave signals. With that in mind, we can add that a lower frequency of events occurs with a thick ice mélange, leading to even fewer recorded events during winter and spring. Interestingly, atmospheric conditions such as foehn winds indirectly increased calving detection by breaking up the ice mélange, allowing more waves to propagate through the fjord, for example, in December 2023 and January 2024. Glacier flow variability, on the contrary, appeared to have no measurable influence on calving frequency or size. With regard to tides, a slight increase in calving events was observed during low tide. Overall, the ice mélange has the most influence among the external forc-

ing factors studied, influencing both the frequency and the detection of calving events. Lastly, the methodological suitability of tide gauges to monitor calving activity was discussed. The hypothesis suggested that, while a tide gauge could provide valuable long-term records, it would be insufficient for a detailed analysis of individual events. Tide gauges were found to be highly effective in recording general trends in calving activity over time. Their affordability, simplicity, and autonomy make them ideal for multi-year monitoring. However, limitations include the difficulty of determining the precise volume of individual ice falls and the difficulty of distinguishing between calving types based only on wave characteristics, even if some patterns can be seen. The influence of ice mélange also reduces their accuracy during certain periods, which is why adding a correction for the thickness of the ice melange when extracting the calving waves could improve their reliability. Despite these limitations, the method offers a valuable component of a broader monitoring strategy. Integrating tide gauges with other observation techniques, such as TRI, seismic monitoring, or time-lapse cameras, can significantly improve the overall reliability of calving monitoring.

In summary, this thesis demonstrates the feasibility and value of tide gauges as a sensor to monitor calving activity over extended periods. The high temporal resolution of the wave height data, combined with a robust detection algorithm, enabled the construction of a comprehensive calving event database. The integration of multiple detection methods further enhanced the reliability of the results and allowed a precise interpretation of the wave records. However, several limitations remain, particularly concerning sensor placement and the dampening effect of ice mélange, which complicates both event detection and wave height estimations. The fact that the algorithm is based on fixed thresholds also introduces uncertainty, particularly when it comes to detecting smaller events. However, the methodology proved sufficient for identifying broad temporal patterns and calving dynamics across seasons and years. Future research should aim to improve spatial precision and detection accuracy through the use of multiple tide gauges for triangulation, which could help estimate calving locations and correct for distance-based signal attenuation. Incorporating signal processing techniques such as Fourier analysis may also uncover patterns that are not visible in the time domain alone. An improved correction for the thickness of the ice mélange within the detection algorithm would enhance event detection during winter and spring, helping mitigate the dampening effect. Given its global importance, particularly in terms of sea level rise and fjord circulation, it is essential to continue the interdisciplinary monitoring of glacier-ocean interactions.

6 Bibliography

Alstott, J., Bullmore, E., & Plenz, D. (2014). *powerlaw: A Python Package for Analysis of Heavy-Tailed Distributions. PLOS ONE*, 9(1), e85777. https://doi.org/10.1371/journal.pone.0085777

Amundson, J. M., Clinton, J. F., Fahnestock, M., Truffer, M., Lüthi, M. P., & Motyka, R. J. (2012). *Observing calving-generated ocean waves with coastal broadband seismometers, Jakobshavn Isbræ, Greenland. Annals of Glaciology*, 53(60), 79–84. https://doi.org/10.3189/2012/AoG60A200

Amundson, J. M., Fahnestock, M., Truffer, M., Brown, J., Lüthi, M. P., & Motyka, R. J. (2010). *Ice mélange dynamics and implications for terminus stability, Jakobshavn Isbræ, Greenland. Journal of Geophysical Research: Earth Surface*, 115(F1). https://doi.org/10.1029/2009JF001405

Bartholomaus, T. C., Larsen, C. F., West, M. E., O'Neel, S., Pettit, E. C., & Truffer, M. (2015). *Tidal and seasonal variations in calving flux observed with passive seismology. Journal of Geophysical Research: Earth Surface*, 120(11), 2318–2337. https://doi.org/10.1002/2015JF003641

Bartholomaus, T. C., Stearns, L. A., Sutherland, D. A., Shroyer, E. L., Nash, J. D., Walker, R. T., Catania, G., Felikson, D., Carroll, D., Fried, M. J., Noël, B. P. Y., & Broeke, M. R. V. D. (2016). *Contrasts in the response of adjacent fjords and glaciers to ice-sheet surface melt in West Greenland. Annals of Glaciology*, 57(73), 25–38. https://doi.org/10.1017/aog.2016.19

Benn, D. I., Cowton, T., Todd, J., & Luckman, A. (2017). *Glacier Calving in Greenland. Current Climate Change Reports*, 3(4), 282–290. https://doi.org/10.1007/s40641-017-0070-1

Benn, D. I., Warren, C. R., & Mottram, R. H. (2007). *Calving processes and the dynamics of calving glaciers. Earth-Science Reviews*, 82(3), 143–179. https://doi.org/10.1016/j.earscirev.2007.02.002

Cassotto, R., Fahnestock, M., Amundson, J. M., Truffer, M., & Joughin, I. (2015). *Seasonal and interannual variations in ice mélange and its impact on terminus stability, Jakobshavn Isbræ, Greenland. Journal of Glaciology*, 61(225), 76–88. https://doi.org/10.3189/2015jog13j235

Catania, G. A., Stearns, L. A., Moon, T. A., Enderlin, E. M., & Jackson, R. H. (2020). *Future Evolution of Greenland's Marine-Terminating Outlet Glaciers. Journal of Geophysical Research: Earth Surface*, 125(2), e2018JF004873. https://doi.org/10.1029/2018JF004873

Catania, G. A., Stearns, L. A., Sutherland, D. A., Fried, M. J., Bartholomaus, T. C., Morlighem, M., Shroyer, E., & Nash, J. (2018). *Geometric Controls on Tidewater Glacier Retreat in Central Western Greenland. Journal of Geophysical Research: Earth Surface*, 123(8), 2024–2038. https://doi.org/10.1029/2017JF004499

Create your own Custom Map — MapChart. (s. d.). *MapChart*. https://www.mapchart.net/index.html

Dachauer, A., Kneib-Walter, A., Gräff, D., & Vieli, A. (2024). *Calving and ice flow variability during a 12-day period using terrestrial radar interferometry.*

Deane, G. B., Glowacki, O., Stokes, M. D., & Pettit, E. C. (2019, December 2). *The Underwater Sounds of Glaciers—Grant B. Deane. Acoustics Today.* https://acousticstoday.org/the-underwater-sounds-of-glaciers-grant-b-deane/

Enderlin, E. M., Howat, I. M., Jeong, S., Noh, M.-J., van Angelen, J. H., & van den Broeke, M. R. (2014). *An improved mass budget for the Greenland ice sheet. Geophysical Research Letters*, 41(3), 866–872. https://doi.org/10.1002/2013GL059010

ITS_LIVE a NASA MEaSURES program — NASA JPL. (s. d.-b). *ITS_LIVE A NASA MEaSURES Program — NASA JPL.* https://its-live.jpl.nasa.gov/

GEUS Dataverse. (s. d.). https://dataverse.geus.dk/

Green Fjord. (n.d.). Retrieved 21 January 2025, from https://greenfjord-project.ch/

Grosfeld, K., Schröder, M., Fahrbach, E., Gerdes, R., & Mackensen, A. (2001). *How iceberg calving and grounding change the circulation and hydrography in the Filchner Ice Shelf-Ocean System. Journal of Geophysical Research: Oceans*, 106(C5), 9039–9055. https://doi.org/10.1029/2000JC000601

Heller, V., Chen, F., Brühl, M., Gabl, R., Chen, X., Wolters, G., & Fuchs, H. (2019). *Large-scale experiments into the tsunamigenic potential of different iceberg calving mechanisms. Scientific Reports*, 9(1), 861. https://doi.org/10.1038/s41598-018-36634-3

Holland, D. M., Voytenko, D., Christianson, K., Dixon, T. H., Mei, M. J., Parizek, B. R., Vaňková, I., Walker, R. T., Walter, J. I., Nicholls, K., & Holland, D. (2016). *An Intensive Observation of Calving at Helheim Glacier, East Greenland. Oceanography (Washington, D.C.)*, 29(4), 46–61. https://doi.org/10.5670/oceanog.2016.98

IPCC. (2019). *The Ocean and Cryosphere in a Changing Climate: Special Report of the Intergovernmental Panel on Climate Change* (1st ed.). Cambridge University Press. https://doi.org/10.1017/9781009157964

Jenkins, W. G., Gunner, J. D., & Young, R. (1980). *Narssarssuaq, South Greenland 1972 and 1976 expedition results.* https://doi.org/10.17863/CAM.31676

Joughin, I., Das, S. B., King, M. A., Smith, B. E., Howat, I. M., & Moon, T. (2008). *Seasonal Speedup Along the Western Flank of the Greenland Ice Sheet. Science*, 320(5877), 781–783. https://doi.org/10.1126/science.1153288

Jouvet, G., Weidmann, Y., Seguinot, J., Funk, M., Abe, T., Sakakibara, D., Seddik, H., & Sugiyama, S. (2017). *Initiation of a major calving event on the Bowdoin Glacier captured by UAV photogrammetry. The Cryosphere*, 11(2), 911–921. https://doi.org/10.5194/tc-11-911-2017

King, M. D., Howat, I. M., Candela, S. G., Noh, M. J., Jeong, S., Noël, B. P. Y., van den Broeke, M. R., Wouters, B., & Negrete, A. (2020). *Dynamic ice loss from the Greenland Ice Sheet driven by sustained glacier retreat. Communications Earth & Environment*, 1(1), 1–7. https://doi.org/10.1038/s43247-020-0001-2

King, M. D., Howat, I. M., Jeong, S., Noh, M. J., Wouters, B., Noël, B., & van den Broeke, M. R. (2018). *Seasonal to decadal variability in ice discharge from the Greenland Ice Sheet. The Cryosphere*, 12(12), 3813–3825. https://doi.org/10.5194/tc-12-3813-2018

Kneib-Walter, A., Lüthi, M. P., Funk, M., Jouvet, G., & Vieli, A. (2023). *Observational constraints on the sensitivity of two calving glaciers to external forcings. Journal of Glaciology*, 69(275), 459–474. https://doi.org/10.1017/jog.2022.74

Kneib-Walter, A., Lüthi, M. P., Moreau, L., & Vieli, A. (2021). *Drivers of Recurring Seasonal Cycle of Glacier Calving Styles and Patterns. Frontiers in Earth Science*, 9. https://doi.org/10.3389/feart.2021.667717

Lüthi, M. P., & Vieli, A. (2016). *Multi-method observation and analysis of a tsunami caused by glacier calving. The Cryosphere*, 10(3), 995–1002. https://doi.org/10.5194/tc-10-995-2016

MacAyeal, D. R., Freed-Brown, J., Zhang, W. W., & Amundson, J. M. (2012). *The influence of ice melange on fjord seiches. Annals of Glaciology*, 53(60), 45–49. https://doi.org/10.3189/2012/AoG60A027

Marchetti, E., Walter, F., & Meier, L. (2021). *Broadband Infrasound Signal of a Collapsing Hanging Glacier. Geophysical Research Letters*, 48(16), e2021GL093579. https://doi.org/10.1029/2021GL093579

Earthdata Search. (s. d.). https://search.earthdata.nasa.gov/search/granules?p=C3177912929-NSIDC_ECS

Millan, R., Rignot, E., Mouginot, J., Wood, M., Bjørk, A. A., & Morlighem, M. (2018). *Vulnerability of Southeast Greenland Glaciers to Warm Atlantic Water From Operation IceBridge and Ocean Melting Greenland Data. Geophysical Research Letters*, 45(6), 2688–2696. https://doi.org/10.1002/2017GL076561

Minowa, M., Podolskiy, E. A., Jouvet, G., Weidmann, Y., Sakakibara, D., Tsutaki, S., Genco, R., & Sugiyama, S. (2019). *Calving flux estimation from tsunami waves. Earth and Planetary Science Letters*, 515, 283–290. https://doi.org/10.1016/j.epsl.2019.03.023

Minowa, M., Podolskiy, E. A., Sugiyama, S., Sakakibara, D., & Skvarca, P. (2018). *Glacier calving observed with time-lapse imagery and tsunami waves at Glaciar Perito Moreno, Patagonia. Journal of Glaciology*, 64(245), 362–376. https://doi.org/10.1017/jog.2018.28

Moltke, C., & Jessen, A. (1896). *Meddelelser Om Grønland*. C.A. Reitzel.

Morlighem, M., Williams, C. N., Rignot, E., An, L., Arndt, J. E., Bamber, J. L., Catania, G., Chauché, N., Dowdeswell, J. A., Dorschel, B., Fenty, I., Hogan, K., Howat, I., Hubbard, A., Jakobsson, M., Jordan, T. M., Kjeldsen, K. K., Millan, R., Mayer, L., ... Zinglersen, K. B. (2017). *BedMachine v3: Complete Bed Topography and Ocean Bathymetry Mapping of Greenland From Multibeam Echo Sounding Combined With Mass Conservation. Geophysical Research Letters*, 44(21), 11,051–11,061. https://doi.org/10.1002/2017GL074954

Mortensen, J., Bendtsen, J., Motyka, R. J., Lennert, K., Truffer, M., Fahnestock, M., & Rysgaard, S. (2013). *On the seasonal freshwater stratification in the proximity of fast-flowing tidewater outlet glaciers in a sub-Arctic sill fjord. Journal of Geophysical Research: Oceans*, 118(3), 1382–1395. https://doi.org/10.1002/jgrc.20134

Mouginot, J., Rignot, E., Bjørk, A. A., Van Den Broeke, M., Millan, R., Morlighem, M., Noël, B., Scheuchl, B., & Wood, M. (2019). *Forty-six years of Greenland Ice Sheet mass balance from 1972 to 2018. Proceedings of the National Academy of Sciences*, 116(19), 9239–9244. https://doi.org/10.1073/pnas.1904242116

Muckenhuber, S., Nilsen, F., Korosov, A., & Sandven, S. (2016). *Sea ice cover in Isfjorden and Hornsund, Svalbard (2000–2014) from remote sensing data. The Cryosphere*, 10(1), 149–158. https://doi.org/10.5194/tc-10-149-2016

Nick, F. M., Vieli, A., Howat, I. M., & Joughin, I. (2009). *Large-scale changes in Greenland outlet glacier dynamics triggered at the terminus. Nature Geoscience*, 2(2), 110–114. https://doi.org/10.1038/ngeo394

Otosaka, I. N., Horwath, M., Mottram, R., & Nowicki, S. (2023). *Mass Balances of the Antarctic and Greenland Ice Sheets Monitored from Space. Surveys in Geophysics*, 44(5), 1615–1652. https://doi.org/10.1007/s10712-023-09795-8

Publikationer og rapporter. (n.d.). DMI. https://www.dmi.dk/publikationer

Rabinovich, A. B. (1997). *Spectral analysis of tsunami waves: Separation of source and topography effects. Journal of Geophysical Research: Oceans*, 102(C6), 12663–12676. https://doi.org/10.1029/97JC00479

RBR. (2024, août 8). *RBR — World leading oceanographic instruments.* https://rbr-global.com/

Rignot, E., & Kanagaratnam, P. (2006). *Changes in the Velocity Structure of the Greenland Ice Sheet. Science*, 311(5763), 986–990. https://doi.org/10.1126/science.1121381

Rignot, E., Velicogna, I., van den Broeke, M. R., Monaghan, A., & Lenaerts, J. T. M. (2011). *Acceleration of the contribution of the Greenland and Antarctic ice sheets to sea level rise. Geophysical Research Letters*, 38(5). https://doi.org/10.1029/2011GL046583

Ryo, M., Leys, M., & Robinson, C. T. (2016). *Technical note: Fourier approach for estimating the thermal attributes of streams. Hydrology and Earth System Sciences*, 20(8), 3411–3418. https://doi.org/10.5194/hess-20-3411-2016

Sentinel Hub. (s. d.). https://www.sentinel-hub.com/

Shepherd, A., Ivins, E., Rignot, E., Smith, B., van den Broeke, M., Velicogna, I., Whitehouse, P., Briggs, K., Joughin, I., Krinner, G., Nowicki, S., Payne, T., Scambos, T., Schlegel, N., A, G., Agosta, C., Ahlstrøm, A., Babonis, G., Barletta, V. R., ... The IMBIE Team. (2020). *Mass balance of the Greenland Ice Sheet from 1992 to 2018. Nature*, 579(7798), 233–239. https://doi.org/10.1038/s41586-019-1855-2

Straneo, F., Heimbach, P., Sergienko, O., Hamilton, G., Catania, G., Griffies, S., Hallberg, R., Jenkins, A., Joughin, I., Motyka, R., Pfeffer, W. T., Price, S. F., Rignot, E., Scambos, T., Truffer, M., & Vieli, A. (2013). *Challenges to Understanding the Dynamic Response of Greenland's Marine Terminating Glaciers to Oceanic and Atmospheric Forcing. Bulletin of the American Meteorological Society*, 94(8), 1131–1144. https://doi.org/10.1175/BAMS-D-12-00100.1

Sugiyama, S., Tsutaki, S., Sakakibara, D., Asaji, I., Kondo, K., Wang, Y., Podolskiy, E., Jouvet, G., & Funk, M. (2025). *Ice speed of a Greenlandic tidewater glacier modulated by tide, melt, and rain. The Cryosphere*, 19(1), 525–540. https://doi.org/10.5194/tc-19-525-2025

Sutherland, D. A., & Pickart, R. S. (2008). *The East Greenland Coastal Current: Structure, variability, and forcing. Progress in Oceanography*, 78(1), 58–77. https://doi.org/10.1016/j.pocean.2007.09.006

van den Broeke, M. R., Enderlin, E. M., Howat, I. M., Kuipers Munneke, P., Noël, B. P. Y., van de Berg, W. J., van Meijgaard, E., & Wouters, B. (2016). *On the recent contribution of the Greenland ice sheet to sea level change. The Cryosphere*, 10(5), 1933–1946. https://doi.org/10.5194/tc-10-1933-2016

Vieli, A., Dachauer, A., Gräff, D., Walter, A., Lipovsky, B., Walter, F., & Welty, E. (2024, March 7). *Multi-sensor approach of monitoring ice-ocean interaction at high resolution at a major ocean-terminating glacier in South Greenland. EGU24.* https://doi.org/10.5194/egusphere-egu24-14713

Vieli, A., Funk, M., & Blatter, H. (2001). *Flow dynamics of tidewater glaciers: A numerical modelling approach. Journal of Glaciology*, 47(159), 595–606. https://doi.org/10.3189/172756501781831747

Vieli, A., & Nick, F. M. (2011). *Understanding and Modelling Rapid Dynamic Changes of Tidewater Outlet Glaciers: Issues and Implications. Surveys in Geophysics*, 32(4), 437–458. https://doi.org/10.1007/s10712-011-9132-4

Walter, A., Lüthi, M. P., & Vieli, A. (2020). *Calving event size measurements and statistics of Eqip Sermia, Greenland, from terrestrial radar interferometry. The Cryosphere*, 14(3), 1051–1066. https://doi.org/10.5194/tc-14-1051-2020

Walter, F., Gräff, D., Lindner, F., Paitz, P., Köpfli, M., Chmiel, M., & Fichtner, A. (2020). *Distributed acoustic sensing of microseismic sources and wave propagation in glaciated terrain. Nature Communications*, 11(1), 2436. https://doi.org/10.1038/s41467-020-15824-6

Wehrlé, A., Lüthi, M. P., & Vieli, A. (2023). *The control of short-term ice mélange weakening episodes on calving activity at major Greenland outlet glaciers. The Cryosphere*, 17(1), 309–326. https://doi.org/10.5194/tc-17-309-2023

Weidick, A. (1995). *Satellite Image Atlas of Glaciers of the World—Greenland.*

Weidick, A. (2009). *Johan Dahl Land, south Greenland: The end of a 20th century glacier expansion. Polar Record*, 45(4), 337–350. https://doi.org/10.1017/S003224740900833X

7 Appendices

Number of Detected Peaks for Various mph and mpd Combinations (p1, p2, p3)

	1200	1100	1000	900	800	700	600	500	400	300	200	100
0.0100	45 67 88	45 68 90	46 71 93	46 78 98	50 79 103	52 82 110	54 90 115	56 94 130	65 102 145	72 114 160	90 138 211	128 222 330
0.0090	46 71 89	46 72 92	48 75 96	48 82 99	52 83 104	55 86 112	57 96 119	60 99 135	69 106 150	76 122 166	94 148 219	135 247 348
0.0080	47 75 92	48 76 93	50 79 97	51 87 101	54 88 107	57 91 115	59 100 122	64 104 139	73 112 155	81 128 172	100 157 228	145 261 372
0.0070	48 77 96	49 79 98	51 84 104	52 89 106	55 91 114	59 96 122	61 105 131	66 108 149	77 117 165	85 136 186	106 165 246	152 279 401
0.0060	48 81 98	49 83 101	51 87 106	53 93 109	56 95 116	60 100 124	62 110 135	68 116 157	79 127 172	89 147 193	110 177 259	163 303 439
0.0050	49 87 106	50 91 108	54 95 113	56 100 118	57 102 125	61 108 137	63 117 149	70 126 171	80 140 184	91 160 212	118 194 284	179 337 477
0.0040	51 93 112	52 98 116	57 102 120	60 105 126	62 108 133	68 117 143	76 129 158	81 138 182	92 153 199	106 174 228	135 215 310	202 368 523
0.0030	53 105 126	55 107 131	59 112 134	61 114 139	65 119 152	73 129 165	82 141 180	88 156 205	100 172 222	119 192 264	152 242 354	230 412 598
0.0020	56 121 144	58 123 147	64 131 153	65 136 160	69 146 176	78 151 192	92 162 207	99 185 231	110 210 265	140 237 318	173 301 433	284 515 718
0.0010	61 142 184	66 148 188	73 157 198	77 162 215	82 173 234	92 185 255	106 207 282	121 230 313	146 254 352	175 300 430	233 391 589	375 677 991
0.0005	68 177 212	73 184 225	77 191 244	84 201 269	89 218 297	104 235 326	117 260 357	135 295 404	168 339 467	201 398 577	280 530 793	454 899 1352
0.0001	78 232 316	82 252 335	88 272 371	98 302 413	115 327 465	129 358 523	150 401 603	177 456 720	215 540 881	273 652 1136	398 887 1621	691 1567 2868

Table 5: *Number of calving events detected depending on the thresholds for P1, P2, and P3. The number of events necessary for each tide gauge after manually counting peaks is highlighted: red for P1, blue for P2, and green for P3.*

Declaration of authenticity

Personal declaration: I hereby declare that the submitted thesis is the result of my own, independent work. All external sources are explicitly acknowledged in the thesis.
I also declare the assistance of AI tools such as ChatGPT and DeepL. These tools were useful in helping me to put my ideas into words and refine my sentences for better understanding, as well as correcting my coding errors.

Zurich May 22, 2025 Antonin Salamin